Symmetrization, Vortex Rossby Waves, And Hurricane Motion In An Asymmetric Balance Model

Randall J. Kallenbach and Michael T. Montgomery

Research Supported by the Office of Naval Research
Grant # ONR N00014-93-1-0456
And by the National Science Foundation
Grant # NSF ATM-9312655.

Colorado State University

DEPARTMENT OF ATMOSPHERIC SCIENCE

PAPER NO. 588

SYMMETRIZATION, VORTEX ROSSBY WAVES, AND HURRICANE MOTION IN AN ASYMMETRIC BALANCE MODEL

Randall J. Kallenbach and Michael T. Montgomery

Research supported by the Office of Naval Research ONR-N00014-93-1-0456 and the National Science Foundation NSF ATM 9312655

Principal Investigator: Michael T. Montgomery

Department of Atmospheric Science

Colorado State University

Fort Collins, CO 80523

June 1995

Atmospheric Science Paper No. 588

ABSTRACT

The complexity of primitive equation (PE) models commonly used for forecasting hurricane track and structure changes can often make interpretation of their output difficult and speculative. A simplified balance formulation of these phenomena is desirable to further understand the physics of rapidly rotating storms. This work presents a shallow-water numerical model suitable for simulating hurricane track and evolution based on asymmetric balance (AB) theory.

The model is a shallow-water formulation of AB, that incorporates rapid rotation and permits order-one divergence. The solution technique employed is a pseudo-spectral azimuthal modes model utilizing grid points radially and Fourier modes azimuthally.

In this work we also consider the process of vortex axisymmetrization as a model for outward–propagating spiral bands in hurricanes. The basic physics is illustrated most simply for stable potential vorticity monopoles on an f-plane. Unlike the dynamics of sheared disturbances in rectilinear shear flow, symmetrizing disturbances on vortex monopoles are accompanied by outward–propagating Rossby waves whose restoring mechanism is associated with the vortex potential vorticity gradient. Expressions for phase and group velocities are derives and verified that confirm early speculations on the existence of vortex Rossby waves in hurricanes. The theory is applied to a hurricane-like vortex and the results are consistent with radar observations. The wave mechanics developed here shows promise in elucidating basic mechanisms of hurricane evolution and structure changes, such as the formation of secondary eyewalls.

ACKNOWLEDGEMENTS

This work was sponsored by the Office of Naval Research ONR-N00014-93-1-0456 and the National Science Foundation NSF ATM-9312655. Mr. Kallenbach was supported through the Air Force Institute of Technology program. Numerical computations were performed using Hewlett Packard (HP) Apollo series computers belonging to the Montgomery Research Project. Programs were written in HP FORTRAN 9000 and in the Interactive Data Language (IDL) of Research Systems, Inc.

CONTENTS

Chapter 1

INTRODUCTION

The complexity of primitive equation (PE) models commonly used for forecasting hurricane track and structure changes can often make interpretation of their output difficult and speculative. A simplified balance formulation of these phenomena is desirable to further understand the physics of rapidly rotating storms. The development of a balance model for hurricanes spanning the inner–core to the environment is generally difficult because of the lack of a clear time–scale separation between advective and gravity–inertia wave processes in the near–core region of an intense vortex. A solution to the scale problem employing a balance model approach was proposed by Shapiro and Montgomery (1993; hereafter SM) as asymmetric balance (AB) theory. The formulation involves an ordered expansion in a local Rossby number that reduces to quasi–geostrophic theory in the environment and Eliassen's (1951) balance vortex model for purely axisymmetric flow. The zeroth–order expansion is formally valid for wavenumber one in the rapidly rotating portion of the vortex. Validation of the zeroth–order truncation for high–wavenumber asymmetries ($n \geq 2$) is a major objective of this study.

In a study of vortex motion, Willoughby (1992) described the positioning errors between the cylindrical grid center and the vortex center as "alpha gyres". The alpha gyres have the same radial structure as the mean tangential wind. In a stationary grid, for the nondivergent barotropic vorticity equation, Smith and Montgomery (1995; hereafter GSM) identified the long–term wavenumber–one solution as the "pseudo mode". Interestingly, the pseudo mode has the same radial structure as the mean tangential wind. Is there significance in the similarity between the alpha gyre and the pseudo mode? If so, will understanding the connection between the two concepts prove useful in understanding vortex motion?

Early weather surveillance radars suggested outward–propagating banded features throughout the hurricane (e.g., Senn and Hiser 1959). More recent radar studies confirm outward–propagating bands near the eyewall (Tuttle and Gall 1995). In addition to observations that identify outward propagation, many observational studies lacking sufficient temporal resolution nonetheless show evolving fine-structure throughout the vortex (e.g., Black and Willoughby 1992; Barnes et.al. 1983). A particularly noteworthy feature of the Black and Willoughby study was the observation that secondary eyewall formation was accompanied by small-scale fluctuations in the tangential wind. These observations raise unanswered questions concerning the existence of fine-scale, outward–propagating waves accompanying the symmetrization process.

In this thesis it proves convenient to define three regions of the vortex. The inner–core is the region inside the Radius of Maximum Wind (RMW). The near–core extends from just inside the RMW to the radius where the basic state potential vorticity (PV) gradient is small. The outer–core region overlaps the near–core and extends into the quasi–geostrophic (QG) regime where the Rossby number is small compared to unity.

Chapter 2

AB FORMULATION IN SHALLOW WATER VORTEX DYNAMICS

2.1 Introduction

The primary challenge of hurricane modeling, dynamics, and forecasting is the disparity of scales involved (Kasahara and Platzman 1963). One approach solves the scale difficulty by using nested grid models (e.g., Shapiro and Ooyama, 1990; Pielke et al., 1992). An alternative and equally useful solution to the scale problem is to apply balance principles that retain the meteorologically significant motions yet filter gravity–inertia waves. The development of a hurricane balance model spanning the entire vortex, from the inner–core to the environment, is difficult, however, due to the lack of a clear time–scale separation between advective and gravity–inertia wave processes in the near–core. SM tackled the scale problem by employing a balance model that is uniformly valid from the rapidly rotating vortex core to the slowly rotating environment. The theory is called AB and was developed for a baroclinic, continuously stratified vortex.

In this thesis AB theory will be developed and validated for shallow water vortex dynamics. Although the physics of the shallow water model is essentially the same as the baroclinic model, it is mathematically simpler and proves useful in elucidating fundamental flow processes in rapidly rotating vortices. To keep the physics simple, we formulate the linear model assuming f–plane and inviscid dynamics. A stationary coordinate system is adopted.

2.2 Governing Equations

The radial momentum, tangential momentum, and continuity equations for the shallow water system in cylindrical coordinates are, respectively,

$$\frac{\partial u}{\partial t} + u\frac{\partial u}{\partial r} + \frac{v}{r}\frac{\partial u}{\partial \lambda} - fv - \frac{v^2}{r} = -\frac{\partial \phi}{\partial r}, \tag{2.1}$$

$$\frac{\partial v}{\partial t} + u\frac{\partial v}{\partial r} + \frac{v}{r}\frac{\partial v}{\partial \lambda} + fu + \frac{uv}{r} = -\frac{1}{r}\frac{\partial \phi}{\partial \lambda}, \tag{2.2}$$

$$\frac{\partial \phi}{\partial t} + u\frac{\partial \phi}{\partial r} + \frac{v}{r}\frac{\partial \phi}{\partial \lambda} + \phi\left(\frac{1}{r}\frac{\partial (ru)}{\partial r} + \frac{1}{r}\frac{\partial v}{\partial \lambda}\right) = 0, \tag{2.3}$$

where r and λ are the radius and azimuth, u and v are the radial and azimuthal winds, f is the constant Coriolis parameter, and ϕ is the geopotential that equals the free–surface height multiplied by gravity.

Since intense atmospheric vortices often exhibit weak asymmetries (SM), linear perturbation theory is applied about an axisymmetric basic state of swirl. Let $u = u'$, $v = \bar{v}(r) + v'$, and $\phi = \bar{\Phi} + \phi'$, where an overbar denotes the circularly symmetric basic state and a prime denotes asymmetric departures from the basic state. Neglecting products of primed quantities and defining the linear derivative operator following the basic state swirl as

$$\frac{D_{\mathrm{v}}}{Dt} = \frac{\partial}{\partial t} + \frac{\bar{v}}{r}\frac{\partial}{\partial \lambda}, \tag{2.4}$$

the linearized momentum and continuity equations become

$$\frac{D_{\mathrm{v}}}{Dt}u' - f\bar{v} - fv' - \frac{\bar{v}^2}{r} - \frac{2\bar{v}}{r}v' = -\frac{\partial}{\partial r}(\bar{\Phi} + \phi'), \tag{2.5}$$

$$\frac{D_{\mathrm{v}}}{Dt}v' + u'\frac{d\bar{v}}{dr} + fu' + \frac{\bar{v}}{r}u' = -\frac{1}{r}\frac{\partial}{\partial \lambda}(\bar{\Phi} + \phi'), \tag{2.6}$$

$$\frac{D_{\mathrm{v}}}{Dt}\phi' + u'\frac{d\bar{\Phi}}{dr} + \bar{\Phi}\left(\frac{1}{r}\frac{\partial (ru')}{\partial r} + \frac{1}{r}\frac{\partial v'}{\partial \lambda}\right) = 0. \tag{2.7}$$

Since the basic state alone must satisfy equations (2.1) – (2.3), the momentum equations imply

$$f\bar{v} + \frac{\bar{v}^2}{r} = \frac{\partial \bar{\Phi}}{\partial r}, \tag{2.8}$$

$$\frac{\partial \bar{\Phi}}{\partial \lambda} = 0. \tag{2.9}$$

The preponderance of observational evidence supports the gradient balance approximation (2.8). As one example, Willoughby (1990b) showed the mean tangential wind for a large sample of Atlantic storms was within 1.5 ms^{-1} of gradient balance.

After substituting the basic state relations (2.8) and (2.9) back into the disturbance equations, the linearized equations simplify to,

$$\frac{D_v}{Dt}u' - \bar{\xi}v' = -\frac{\partial \phi'}{\partial r}, \tag{2.10}$$

$$\frac{D_v}{Dt}v' + \bar{\eta}u' = -\frac{1}{r}\frac{\partial \phi'}{\partial \lambda}, \tag{2.11}$$

and

$$\frac{D_v}{Dt}\phi' + \bar{\Phi}\left(\frac{1}{r}\frac{\partial (ru')}{\partial r} + \frac{1}{r}\frac{\partial v'}{\partial \lambda}\right) + u'\frac{d\bar{\Phi}}{dr} = 0. \tag{2.12}$$

In (2.10)–(2.12), f denotes a constant Coriolis parameter, $\bar{\zeta} = r^{-1}\, d(r\bar{v})/dr$ the basic state relative vorticity, $\bar{\eta} = f + \bar{\zeta}$ the basic state absolute vorticity, $\bar{\xi} = f + 2\bar{v}/r$ the inertia parameter, and $\bar{\Omega} = \bar{v}/r$ the basic state angular velocity.

2.3 AB Formulation

The AB shallow water formulation parallels the continuously stratified, baroclinic formulation of SM. The shallow water formulation may be thought to result from taking $\partial/\partial z = 0$ and replacing N^2 by $g^2\bar{\Phi}^{-1}$

Instead of taking $\vec{\nabla}\cdot$ and $\vec{\nabla}\times$ of equations (2.10) and (2.11) and neglecting the divergence tendency, we follow the approach of SM and neglect gravity–inertia waves at the momentum level. The gravity–inertia waves are revealed upon differentiating (2.10) and (2.11) with respect to $\frac{D_v}{Dt}$ and cross substituting. The result is an equivalent set of momentum equations in the radial and azimuthal directions, respectively,

$$\left(\frac{D_v{}^2}{Dt^2} + \bar{\eta}\bar{\xi}\right)u' = -\frac{\bar{\xi}}{r}\frac{\partial \phi'}{\partial \lambda} - \frac{D_v}{Dt}\left(\frac{\partial \phi'}{\partial r}\right) \tag{2.13}$$

and

$$\left(\frac{D_v{}^2}{Dt^2} + \bar{\eta}\bar{\xi}\right)v' = -\bar{\eta}\frac{\partial \phi'}{\partial r} - \frac{D_v}{Dt}\left(\frac{1}{r}\frac{\partial \phi'}{\partial \lambda}\right). \tag{2.14}$$

Here $\frac{D_v{}^2}{Dt^2}$ represents a generalized acceleration operator. Equations (2.13) and (2.14) are therefore qualitatively similar to the forced harmonic oscillator with $\bar{\eta}\bar{\xi}$ serving as an

effective spring constant. When the forcing frequency is smaller compared to the intrinsic frequency, we expect that the acceleration term may be neglected.

The scaling of $\frac{D_V{}^2}{Dt^2}$ is the key to filtering the gravity–inertia waves on a rapidly rotating vortex. SM scale $\frac{D_V{}^2}{Dt^2}$ with the advective time scale,

$$\frac{D_V{}^2}{Dt^2} \sim n^2 \frac{\bar{v}^2}{r^2} \tag{2.15}$$

where n is the azimuthal wavenumber. It then proves convenient to define

$$\mathcal{D}^2 = \frac{\frac{D_V{}^2}{Dt^2}}{\bar{\eta}\bar{\xi}} \tag{2.16}$$

and from equation (2.15) we see

$$\mathcal{D}^2 \sim \frac{n^2\bar{v}^2/r^2}{\bar{\eta}\bar{\xi}} \equiv R_n^2, \tag{2.17}$$

the square of the local Rossby number for wavenumber n. The smallness of the local Rossby number then justifies neglecting the acceleration term in equations (2.13) and (2.14).

As the basis of the AB formulation, it is instructive to examine the effect the tangential wind profile has on the magnitude of R_n^2. The "stiffness" of the system, and equivalently the frequency of the unforced response, increases with increasing inertial stability

$$\bar{\eta}\bar{\xi} = f(f + 2\bar{\Omega} + \bar{\zeta}) + 2\bar{\Omega}\bar{\zeta}. \tag{2.18}$$

The vortex is inertially stable when $\bar{\eta}\bar{\xi} > 0$. Substituting (2.18) into (2.17) elucidates the importance of the symmetric wind structure in determining the size of R_n^2. The result is

$$\frac{1}{R_n^2} = \frac{1}{n^2}\left[f\left(\frac{f}{\bar{\Omega}^2} + \frac{3}{\bar{\Omega}} + \frac{1}{\bar{\Omega}^2}\frac{d\bar{v}}{dr}\right) + 2\left(1 + \frac{1}{\bar{\Omega}}\frac{d\bar{v}}{dr}\right)\right]. \tag{2.19}$$

The effect of the vortex structure may be readily illustrated for tangential wind profiles of the form, $\bar{v} = ar^{-b}$, with $a > 0$ for a cyclonic vortex. SM show that for rapidly rotating vortices, R_n^2 is independent of the magnitude of $\bar{v}$, so without loss of generality we may set $a = 1$. With the assumed structure of $\bar{v}$, equation (2.19) becomes

$$\frac{1}{R_n^2} = \frac{1}{n^2}\left[f\left(fr^{(b+1)} + (3-b)\right)r^{(b+1)} + 2(1-b)\right]. \tag{2.20}$$

For $f = 0$, the vortex is inertially unstable for $b > 1$; the vortex is inertially neutral for $b = 1$; while the vortex is inertially stable for $b < 1$. Intense vortex evolution is therefore *not* amenable to a balance model formulation with $b > 1$. For inertially stable vortices ($b < 1$), equation (2.20) shows the presence of f further increases the inertial stability which serves to decrease R_n^2.

In the inner–core, the hurricane is in approximate solid body rotation. With $b = -1$ and $f = 0$, equation (2.20) simplifies to $R_n^2 = \frac{n^2}{4}$. In particular for $n = 1$, $R_1^2 < 1$.

Riehl (1963) and Pearce (1993) suggest a simple reason for why the decay exponent satisfies $0 < b \leq 1/2$ outside the RMW in hurricanes and typhoons. In order for PV to remain unchanged outside the eyewall region, the curl of the frictional force on theta surfaces must vanish. Assuming quadratic surface drag then implies $\bar{v} \propto r^{-1/2}$ for a steady state vortex. For $f = 0$ and $b = 1/2$, equation (2.20) simplifies to $R_n^2 = n^2$. Any positive value of f will then make $R_1^2 < 1$. For observed and theoretical tangential velocity profiles with $-1 < b \leq 1/2$ and realistic values of f, the series should converge for wavenumber one (cf. figure 3 of SM).

The n^2 dependence of R_n^2 suggests the possible divergence of the asymptotic series for high wavenumbers. An important objective of this work is to examine the consistency of the AB formulation in the evolution of high wavenumber asymmetries on a stable hurricane–like vortex, explored at length in chapter 3.

From the definition of $\mathcal{D}^2$, equations (2.13) and (2.14) can be formally written as

$$u' = \frac{\mathcal{I}}{\mathcal{I} + \mathcal{D}^2} \underbrace{\left[-\frac{1}{\bar{\eta} r} \frac{\partial \phi'}{\partial \lambda} - \frac{1}{\bar{\eta} \bar{\xi}} \frac{D_{\mathrm{v}}}{Dt} \left(\frac{\partial \phi'}{\partial r} \right) \right]}_{u'_{\mathrm{o}}}, \tag{2.21}$$

$$v' = \frac{\mathcal{I}}{\mathcal{I} + \mathcal{D}^2} \underbrace{\left[\frac{1}{\bar{\xi}} \frac{\partial \phi'}{\partial r} - \frac{1}{\bar{\eta} \bar{\xi}} \frac{D_{\mathrm{v}}}{Dt} \left(\frac{1}{r} \frac{\partial \phi'}{\partial \lambda} \right) \right]}_{v'_{\mathrm{o}}}, \tag{2.22}$$

where $\mathcal{I}$ is the identity operator. As long as $\mathcal{D}^2 < 1$ the binomial theorem for linear operators allows us to expand equations (2.21) and (2.22) in a series,

$$u' = u'_{\mathrm{o}} - \mathcal{D}^2 u'_{\mathrm{o}} + \left(\mathcal{D}^2 \right)^2 u'_{\mathrm{o}} - \ldots \tag{2.23}$$

and

$$v' = v'_\circ - \mathcal{D}^2 v'_\circ + \left(\mathcal{D}^2\right)^2 v'_\circ - \ldots \quad . \tag{2.24}$$

For simplicity, this work focuses exclusively on the zeroth–order term in the series and the zero subscript will be dropped. This zeroth–order truncation will henceforth be referred to as Asymmetric Balance (AB).

The polarization equations for the balanced wind components are:

$$u' = \underbrace{\overbrace{-\frac{1}{\bar{\eta} r}\frac{\partial \phi'}{\partial \lambda}}^{u'_\eta}}_{\text{"Geostrophic"}} \underbrace{-\frac{1}{\bar{\eta}}\frac{D_\mathrm{v}}{Dt}\overbrace{\left(\frac{1}{\bar{\xi}}\frac{\partial \phi'}{\partial r}\right)}^{v'_\xi}}_{\text{"Isallobaric"}}, \tag{2.25}$$

and

$$v' = \underbrace{\overbrace{\frac{1}{\bar{\xi}}\frac{\partial \phi'}{\partial r}}^{v'_\xi}}_{\text{"Geostrophic"}} \underbrace{+\frac{1}{\bar{\xi}}\frac{D_\mathrm{v}}{Dt}\overbrace{\left(-\frac{1}{\bar{\eta} r}\frac{\partial \phi'}{\partial \lambda}\right)}^{u'_\eta}}_{\text{"Isallobaric"}}. \tag{2.26}$$

The "Geostrophic" and "Isallobaric" terms are generalizations of the geostrophic wind and isallobaric wind from QG theory (cf. Gill 1982).

A useful diagnostic equation comes in the form of the geopotential tendency equation which is the forecast equation for the AB system. Substituting (2.25) and (2.26) into (2.12) gives,

$$\frac{D_\mathrm{v}}{Dt}\phi' + \bar{\Phi}\left[\frac{1}{r}\frac{\partial}{\partial r}\left(-\frac{1}{\bar{\eta}}\phi'_\lambda - \frac{r}{\bar{\eta}\bar{\xi}}\frac{D_\mathrm{v}}{Dt}\phi'_r\right) + \frac{1}{r}\frac{\partial}{\partial \lambda}\left(\frac{1}{\bar{\xi}}\phi'_r - \frac{1}{\bar{\eta}\bar{\xi}}\frac{D_\mathrm{v}}{Dt}\left\{\frac{\phi'_\lambda}{r}\right\}\right)\right] + \left(-\frac{1}{r\bar{\eta}}\phi'_\lambda - \frac{1}{\bar{\eta}\bar{\xi}}\frac{D_\mathrm{v}}{Dt}\phi'_r\right)\frac{d\bar{\Phi}}{dr} = 0, \tag{2.27}$$

with subscripts r and λ denoting partial differentiation. Expanding terms involving mixed partials of ϕ' results in

$$\frac{D_\mathrm{v}}{Dt}\phi' + \bar{\Phi}\left[\frac{1}{r}\frac{d\bar{\eta}}{dr}\frac{\phi'_\lambda}{\bar{\eta}^2}\underbrace{-\frac{\phi'_{r\lambda}}{\bar{\eta} r} + \frac{\phi'_{r\lambda}}{\bar{\xi} r} - \frac{\phi'_{r\lambda}}{\bar{\eta}\bar{\xi}}\frac{d}{dr}\left(\frac{\bar{v}}{r}\right)}_{}\right] - \frac{D_\mathrm{v}}{Dt}\left(\frac{1}{r}\frac{\partial}{\partial r}\left\{\frac{r\phi'_r}{\bar{\eta}\bar{\xi}}\right\} + \frac{\phi'_{\lambda\lambda}}{r^2\bar{\eta}\bar{\xi}}\right)\Bigg] + \left(-\frac{\phi'_\lambda}{\bar{\eta} r} - \frac{1}{\bar{\eta}\bar{\xi}}\frac{D_\mathrm{v}}{Dt}\phi'_r\right)\frac{d\bar{\Phi}}{dr} = 0. \tag{2.28}$$

The swirl identity, $\bar{\xi} - \bar{\eta} = -r d\bar{\Omega}/dr$, simplifies the under–braced terms involving $\phi'_{r\lambda}$ to zero:

$$\begin{aligned}
\phi'_{r\lambda}\left[-\frac{1}{r\bar{\eta}} + \frac{1}{1}r\bar{\xi} - \frac{1}{\bar{\eta}\bar{\xi}}\frac{d}{dr}\left(\frac{\bar{v}}{r}\right)\right] = \\
\frac{\phi'_{r\lambda}}{r\bar{\eta}\bar{\xi}}\left[\bar{\eta} - \bar{\xi} - r\frac{d}{dr}\left(\frac{\bar{v}}{r}\right)\right] = \\
\frac{\phi'_{r\lambda}}{r\bar{\eta}\bar{\xi}}\left[r\frac{d}{dr}\left(\frac{\bar{v}}{r}\right) - r\frac{d}{dr}\left(\frac{\bar{v}}{r}\right)\right] = 0. \qquad (2.29)
\end{aligned}$$

The appropriate inverse square of the Rossby deformation radius is $\bar{\gamma}^2 = \bar{\eta}\bar{\xi}/\bar{\Phi}$. Upon defining the basic state potential vorticity as $\bar{q} = \bar{\eta}/\bar{\Phi}$, and multiplying (2.28) by $\bar{\gamma}^2$ gives a compact geopotential tendency equation:

$$\frac{D_V}{Dt}\left[\frac{\bar{\gamma}^2}{r}\frac{\partial}{\partial r}\left(\frac{r}{\bar{\gamma}^2}\frac{\partial\phi'}{\partial r}\right) + \frac{1}{r^2}\frac{\partial^2\phi'}{\partial\lambda^2} - \bar{\gamma}^2\phi'\right] - \frac{\bar{\xi}}{r\bar{q}}\frac{\partial\phi'}{\partial\lambda}\frac{d\bar{q}}{dr} = 0. \qquad (2.30)$$

In (2.30), $\frac{D_V}{Dt}$ acts on a second–order differential operator $\nabla^2_{AB} - \bar{\gamma}^2$ defined as

$$\left(\nabla^2_{AB} - \bar{\gamma}^2\right) = \frac{\bar{\gamma}^2}{r}\frac{\partial}{\partial r}\left(\frac{r}{\bar{\gamma}^2}\frac{\partial}{\partial r}\right) + \frac{1}{r^2}\frac{\partial^2}{\partial\lambda^2} - \bar{\gamma}^2. \qquad (2.31)$$

If the vortex is inertially stable ($\bar{\eta}\bar{\xi} > 0$), the operator $\nabla^2_{AB} - \bar{\gamma}^2$ is elliptic and unique solutions are guaranteed. Also significant is the parameter $\bar{\gamma}^2$ which provides a smooth transition from the rapidly rotating regime of the inner–core to the slowly rotating environment.

The forecast equation results upon expanding $\frac{D_V}{Dt}$, and isolating $\partial\phi'/\partial t$. The result is

$$\frac{\partial\phi'}{\partial t} = \left(\nabla^2_{AB} - \bar{\gamma}^2\right)^{-1}\left[\frac{\bar{\xi}}{r\bar{q}}\frac{\partial\phi'}{\partial\lambda}\frac{d\bar{q}}{dr} - \frac{\bar{v}}{r}\left(\nabla^2_{AB} - \bar{\gamma}^2\right)\frac{\partial\phi'}{\partial\lambda}\right]. \qquad (2.32)$$

Knowing ϕ' at $t = 0$ along with boundary conditions for $\partial\phi'/\partial t$ allows ϕ' to be stepped forward in time.

2.4 Analogous Conservation Laws

As a verification of formal consistency, several conservation laws analogous to those of the linearized PE may be derived.

2.4.1 Momentum

Multiplying (2.26) by $\bar{\xi}$ and (2.25) by $\bar{\eta}$ gives the radial and azimuthal pseudo–momentum equations, respectively:

$$\frac{D_{\mathrm{v}}}{Dt}u'_\eta - \bar{\xi}v' = -\frac{\partial\phi'}{\partial r} \tag{2.33}$$

$$\frac{D_{\mathrm{v}}}{Dt}v'_\xi + \bar{\eta}u' = -\frac{1}{r}\frac{\partial\phi'}{\partial\lambda}. \tag{2.34}$$

2.4.2 Energy

A disturbance energy equation follows upon forming the combination,

$$\frac{\bar{\Phi}}{g}\left(u'_\xi \times (2.33) + v'_\eta \times (2.34)\right) + \frac{\phi'}{g} \times (2.12), \tag{2.35}$$

to yield,

$$\frac{D_{\mathrm{v}}}{Dt}\underbrace{\left[\frac{\bar{\Phi}}{2g}\left(u'_\xi u'_\eta + v'_\xi v'_\eta\right) + \frac{(\phi')^2}{2g}\right]}_{\text{Term A}} + \underbrace{\frac{\phi'}{g}\left[\frac{1}{r}\frac{\partial}{\partial r}\left(r\bar{\Phi}u'\right) + \frac{1}{r}\frac{\partial\bar{\Phi}v'}{\partial\lambda}\right]}_{\text{Term B}}$$
$$\underbrace{+\frac{\bar{\Phi}}{g}\left[\bar{\eta}u'v'_\eta - \bar{\xi}v'u'_\xi\right]}_{\text{Term C}} + \underbrace{\frac{\bar{\Phi}}{g}\left[u'_\xi\frac{\partial\phi'}{\partial r} + \frac{v'_\eta}{r}\frac{\partial\phi'}{\partial\lambda}\right]}_{\text{Term D}} = 0. \tag{2.36}$$

Term A represents the disturbance energy (kinetic plus potential) integrated over the fluid depth. Terms B and C combine to

$$\nabla\cdot\left(\frac{\bar{\Phi}}{g}\phi'\vec{\mathbf{u}}'\right), \tag{2.37}$$

a depth integrated pressure work term. Recalling the swirl identity simplifies term D to

$$\frac{\bar{\Phi}}{g}v'_\xi u'_\eta r\frac{d\bar{\Omega}}{dr}, \tag{2.38}$$

a depth integrated Reynolds stress. Integration over the entire vortex then gives a bulk measure of the asymmetries. Assuming $\phi'\vec{\mathbf{u}}' \to 0$ as $r \to \infty$ and recalling $\phi'(r=0) = 0$, the boundary terms vanish leaving

$$\frac{\partial}{\partial t}\int_0^{2\pi}\int_0^{\infty}\left[\frac{\bar{\Phi}}{2g}\left(u'_\xi u'_\eta + v'_\xi v'_\eta\right) + \frac{(\phi')^2}{2g}\right] r\,dr\,d\lambda = -\int_0^{2\pi}\int_0^{\infty}\left[\frac{\bar{\Phi}}{g}v'_\xi u'_\eta r\frac{d\bar{\Omega}}{dr}\right] r\,dr\,d\lambda. \tag{2.39}$$

A useful model diagnostic is therefore the integrated disturbance energy

$$E(t) = \int_0^{2\pi}\int_0^{\infty}\left[\frac{\bar{\Phi}}{2g}\left(u'_\xi u'_\eta + v'_\xi v'_\eta\right) + \frac{(\phi')^2}{2g}\right] r\,dr\,d\lambda. \tag{2.40}$$

2.4.3 *Potential Vorticity*

As a further check on the formal consistency of the AB shallow water formulation, a PV conservation principle may also be derived. Expanding $\partial/\partial r$ and grouping terms in equation (2.30) gives,

$$\frac{D_v}{Dt}\left\{\bar{\xi}\left[\frac{1}{r}\frac{\partial}{\partial r}\left(\frac{r}{\bar{\xi}}\frac{\partial\phi'}{\partial r}\right)-\frac{1}{r}\frac{\partial}{\partial\lambda}\left(\frac{-1}{r\bar{\xi}}\frac{\partial\phi'}{\partial\lambda}\right)\right]-\bar{\gamma}^2\phi'\right\}$$
$$+\frac{D_v}{Dt}\left\{\frac{\partial\phi'}{\partial r}\left[\frac{1}{\bar{\xi}}\frac{\partial\bar{\xi}}{\partial r}-\frac{1}{\bar{\gamma}^2}\frac{\partial\bar{\gamma}^2}{\partial r}\right]\right\}-\frac{\bar{\xi}}{r\bar{q}}\frac{\partial\phi'}{\partial\lambda}\frac{d\bar{q}}{dr}=0. \tag{2.41}$$

In analogy with SG theory, it proves convenient to define a pseudo–momentum per unit mass

$$\vec{\mathbf{u}}'_\xi=\left(\frac{-1}{r\bar{\xi}}\frac{\partial\phi'}{\partial\lambda},\frac{1}{\bar{\xi}}\frac{\partial\phi'}{\partial r}\right), \tag{2.42}$$

along with a corresponding vertical vorticity,

$$\zeta'_\xi=\hat{\mathbf{k}}\cdot\nabla\times\vec{\mathbf{u}}'_\xi. \tag{2.43}$$

On dividing equation (2.41) by $\bar{\xi}\bar{\Phi}$, and using the definitions for ζ'_ξ and $\bar{q}$, the forecast equation may be succinctly expressed as a linearized conservation law for pseudo PV

$$\frac{D_v}{Dt}q'_\xi+u'\frac{d\bar{q}}{dr}=0, \tag{2.44}$$

where

$$q'_\xi=\frac{\zeta'_\xi}{\bar{\xi}}-\bar{q}\frac{\phi'}{\bar{\Phi}} \tag{2.45}$$

is the pseudo PV and u' is gotten from (2.25). The definition for q'_ξ is analogous to disturbance PV in the linearized PE shallow water model. The first term represents the flow component of PV and the second term represents the mass component.

2.4.4 *Vorticity*

The AB vorticity equation follows upon taking the horizontal curl of the pseudo–momentum equations, (2.33,2.34):

$$\frac{D_v}{Dt}\zeta'_\xi+u'\frac{d\bar{\eta}}{dr}=-\bar{\eta}\left[\frac{1}{r}\frac{\partial}{\partial r}(ru')+\frac{1}{r}\frac{\partial v'}{\partial\lambda}\right]. \tag{2.46}$$

2.5 Summary

The AB shallow water formulation presented above parallels the baroclinic formulation of SM. The formulation is mathematically simple yet will be shown to effectively illustrate fundamental processes in rapidly rotating vortices. The formal consistency of the AB formulation was demonstrated by formulating conservation laws and diagnostic equations analogous to those of the linearized PE system. These analogous formulations include a geopotential tendency equation, pseudo–momentum equations, an energy equation, potential vorticity conservation, and a vorticity equation.

For the balance formulation to be useful, however, the consistency of the zeroth–order dynamics must be demonstrated for high–wavenumber asymmetries.

Chapter 3

AB VALIDATION THROUGH SYMMETRIZATION

3.1 Introduction

This chapter demonstrates the consistency of the AB formulation in forecasting high wavenumber ($n \geq 2$) asymmetries on a stable hurricane vortex. The need for this demonstration was foreshadowed in section 2.3 where the basis of the AB approximation, $\frac{D_V{}^2}{Dt^2} \ll \bar{\eta}\,\bar{\xi}$, hinged on the smallness of the local Rossby number squared

$$R_n^2 = \frac{n^2\bar{v}^2/r^2}{\bar{\eta}\bar{\xi}}, \tag{3.1}$$

where n denotes the azimuthal wavenumber.

Based on observations of hurricane Gloria (1985), SM showed that the local Rossby number for wavenumber one is less than unity throughout the hurricane vortex. The series expansion should therefore converge for wavenumber one. For hypothetical cases of high wavenumber excitation, the n^2 dependence of R_n^2 suggests the local Rossby number expansion may indeed diverge. Figure 3.1 illustrates the dependence of R_n^2 on n^2 and $\bar{v}(r)$ for the benchmark hurricane–like vortex discussed in further detail in section 3.2. Such considerations together with the knowledge of the behavior of sheared disturbances lead SM to speculate high wavenumber asymmetries would nevertheless be rapidly damped through vortex axisymmetrization and the zeroth–order balance formulation would still correctly predict the eddy–momentum and eddy–heat flux effects on the mean vortex. In this chapter we take the first step towards this by examining the linearized dynamics for azimuthal wavenumbers $n \geq 2$.

The source for high wavenumber asymmetries in hurricanes is continuous forcing by environmental and/or internal processes. To illustrate, a Taylor series expansion about the

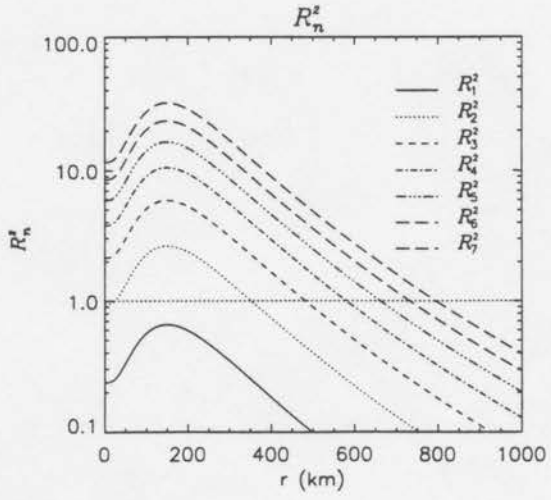

Figure 3.1: Local Rossby number squared for azimuthal wavenumbers one through seven for the benchmark vortex. Note the logarithmic scale on the y–axis. Only the inner 1000 km of the 3000 km domain are shown.

center of the vortex (Willoughby 1992) reveals that a horizontal deformation flow projects onto wavenumber two, while a deformation gradient flow projects onto wavenumber three. Small–scale cumulus convection, on the other hand, is believed to excite a continuum of responses. The cold wake in SSTs caused by Ekman pumping in the oceanic boundary layer projects onto a wavenumber two component by altering the strength of convection at certain locations. These are just a few of the various asymmetric forcings that act on a hurricane during its life cycle. As a first step towards understanding the evolution of high wavenumber asymmetries that are continuously forced, this work assumes a quiescent environment at the boundaries and examines the evolution of asymmetric conditions from the perspective of an initial value problem.

3.2 The Vortex Model

To meet the stated objectives of this chapter, the benchmark vortex will possess large Rossby numbers. The vortex is then initialized with asymmetric disturbances $2 \leq n \leq 7$ on an f–plane whose maximum amplitude resides near the maximum of R_n^2. For the linear formulation considered in this section, the benchmark vortex will remain stationary for the duration of each model run.

3.2.1 The Basic State

As discussed in chapter 2, the circular vortex is assumed to be in gradient wind balance. Consequently the basic state geopotential and related quantities are functions of r only. Gradient balance,

$$\frac{d\bar{\Phi}}{dr} = f\bar{v} + \frac{\bar{v}^2}{r}, \tag{3.2}$$

and the definition of the basic state PV,

$$\bar{q} = \frac{\bar{\eta}}{\bar{\Phi}} = \frac{f + \bar{v}/r + d\bar{v}/dr}{\bar{\Phi}}, \tag{3.3}$$

allows one to uniquely characterize the basic state by specifying $\bar{v}$, $\bar{q}$, or $\bar{\Phi}$.

In order to guarantee both inertial and shear stability in the slow manifold, we restrict attention to monotonically decreasing, infinitely differentiable, positive functions for $\bar{q}(r)$. The $\bar{q}$ profile chosen for the benchmark vortex results in a tangential wind profile $\bar{v} \propto r^{-1/2}$ in the outer–core region of the vortex. This tangential wind profile satisfies the conditions for a quasi–steady vortex under the effects of surface friction, (Riehl 1963; Pearce 1993; Willoughby 1990a). This profile also ensures that $R_1^2 < 1$ throughout the vortex. The benchmark vortex scales as a minimal hurricane with the maximum tangential wind of 36.8 ms^{-1} located at 75 km. The model setup assumes a resting depth of 1 km, a Coriolis parameter $f = 5 \times 10^{-5} s^{-1}$, and an outer boundary of 3000 km. Figure 3.2 shows the inner 1000 km of several basic state quantities. The deformation radius in the inner–core region is 41.4 km, a value consistent with the first internal mode for hurricanes. Figure 3.1 shows that R_n^2 is large in the near–core region for wavenumbers $2 \leq n \leq 7$.

3.2.2 Initial Conditions

The initial geopotential necessary to begin the model forecast is obtained from the disturbance PV using the invertibility relationship of the AB formulation. Letting $\hat{}$ denote the azimuthal–Fourier transform, the invertibility equation is

$$\hat{q}_\xi = \frac{1}{\bar{\Phi}} \frac{\partial}{r\partial r}\left(\frac{r}{\bar{\xi}} \frac{\partial \hat{\phi}}{\partial r}\right) - \frac{n^2}{r^2} \frac{1}{\bar{\xi}} \frac{\hat{\phi}}{\bar{\Phi}} - \bar{q} \frac{\hat{\phi}}{\bar{\Phi}}. \tag{3.4}$$

For a given radial structure of $\hat{q}_\xi$, (3.4) is solved for $\hat{\phi}$ using a tridiagonal solver assuming that $\hat{\phi}$ vanishes at both $r = 0$ and $r = r_{max}$. The n^2 dependence in the invertibility

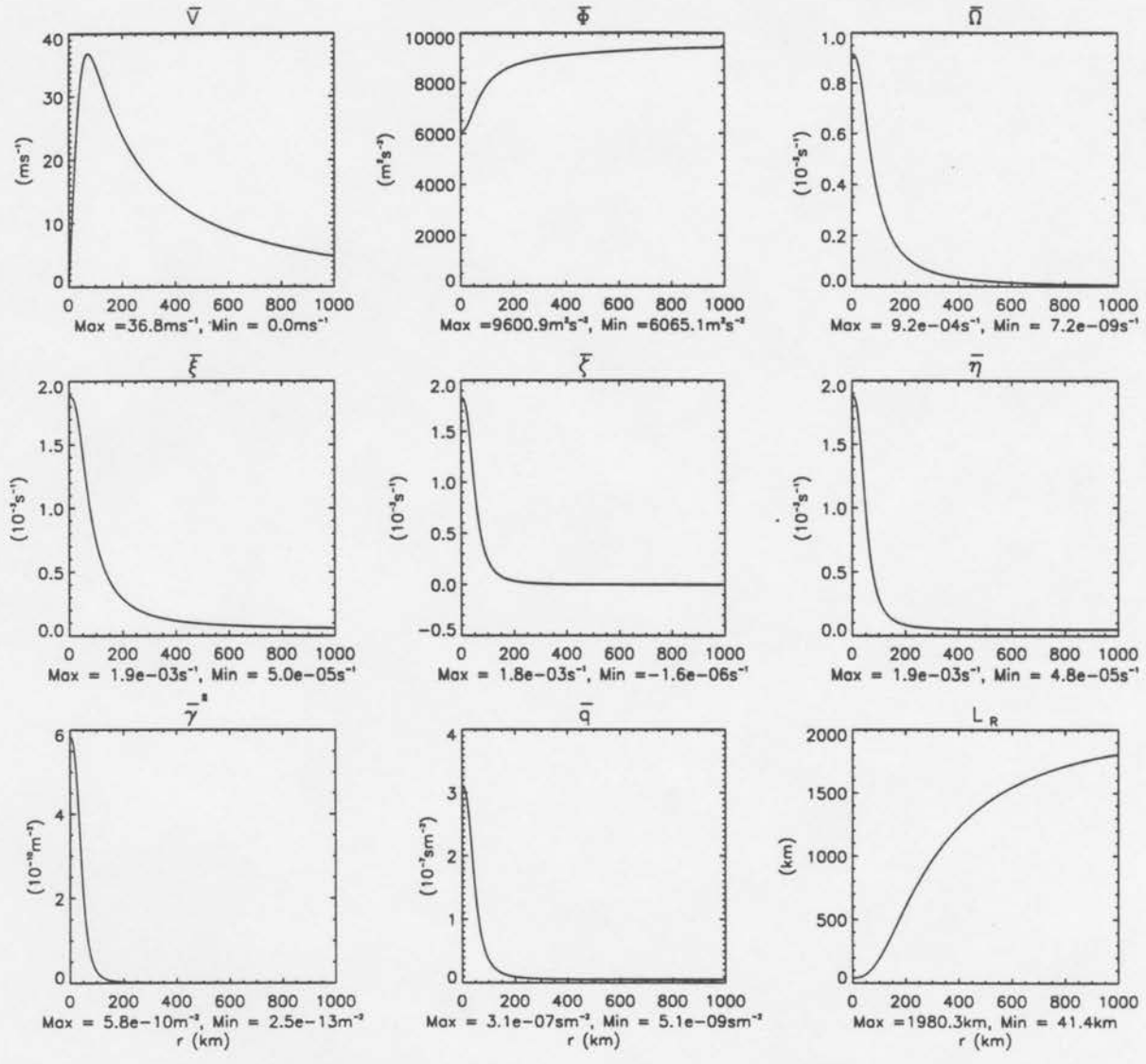

Figure 3.2: The benchmark vortex: $\bar{v}$ the tangential wind; $\bar{\Phi}$ the geopotential for a fluid with a resting depth of 1 km; $\bar{\Omega}$ the storm rotation rate; $\bar{\xi}$ the inertia parameter; $\bar{\zeta}$ the relative vorticity; $\bar{\eta}$ the absolute vorticity for $f = 5 \times 10^{-5} s^{-1}$; $\bar{\gamma}^2$ the inverse deformation radius squared; $\bar{q}$ the potential vorticity $= \bar{\eta}/\bar{\Phi}$; and L_R the deformation radius. Only the inner 1000 km of the 3000 km domain are shown.

problem implies that for similar PV disturbances, both the amplitude and the radial extent of the geopotential response will decrease with n^2.

To ensure that disturbance PV is continuous at the origin, $\hat{q}_\xi$ must vanish at $r = 0$ for $n \geq 1$. The family of horizontally–upright initial conditions given by

$$\hat{q}_\xi(r) = A_o \times r^n \times \exp(-\alpha r^n) \tag{3.5}$$

satisfies this requirement, where $\alpha > 0$ and A_o is the perturbation amplitude. This initial condition is less convenient than horizontally–upright Gaussians of the form

$$\hat{q}_\xi(r) = A_o \times \exp(-(\frac{r - r_{peak}}{r_{fold}})^2), \tag{3.6}$$

where r_{peak} is the radius of maximum amplitude, and r_{fold} is the e–folding distance. Despite the resulting PV–discontinuity at $r = 0$, the invertibility problem forces the disturbance geopotential to vanish as r^n. The coresponding perturbation heights, wind fields, and energy densities are therefore continuous throughout the flow. Because (3.6) permits side–by–side comparisons with other research models (e.g. GSM), (3.6) was used throughout this work. Results shown below were subsequently verified with the smoother initial conditions of (3.5).

The vortex is initialized with the identical radial structure of $\hat{q}_\xi$ for wavenumbers two through seven using $r_{peak} = 75\ km$ (the RMW), $A_o = 2 \times 10^{-8} sm^{-2}$ (7% of the basic state), and $r_{fold} = 75\ km$ (the characteristic scale of the vortex). Figure 3.3 shows map plots of q'_ξ and ϕ' for wavenumbers two through four. As evident from figure 3.1, the asymmetries are placed in a region where $R_n^2 \gg 1$. Not shown are plots of wavenumbers five through seven which exhibit similar qualitative relationships between q'_ξ and ϕ'. Figure 3.4 shows the radial profile of $|\hat{q}_\xi|$ and the resulting $\left|\hat{\phi}\right|$ profile for wavenumbers two through four. Similar to the map plots, the radial plots confirm the solution dependence on n^2.

3.3 Inner–Core Symmetrization

Analytical models are extremely useful for demonstrating and quantifying the inviscid physics of symmetrization since they avoid the complexities of time–stepping schemes. The

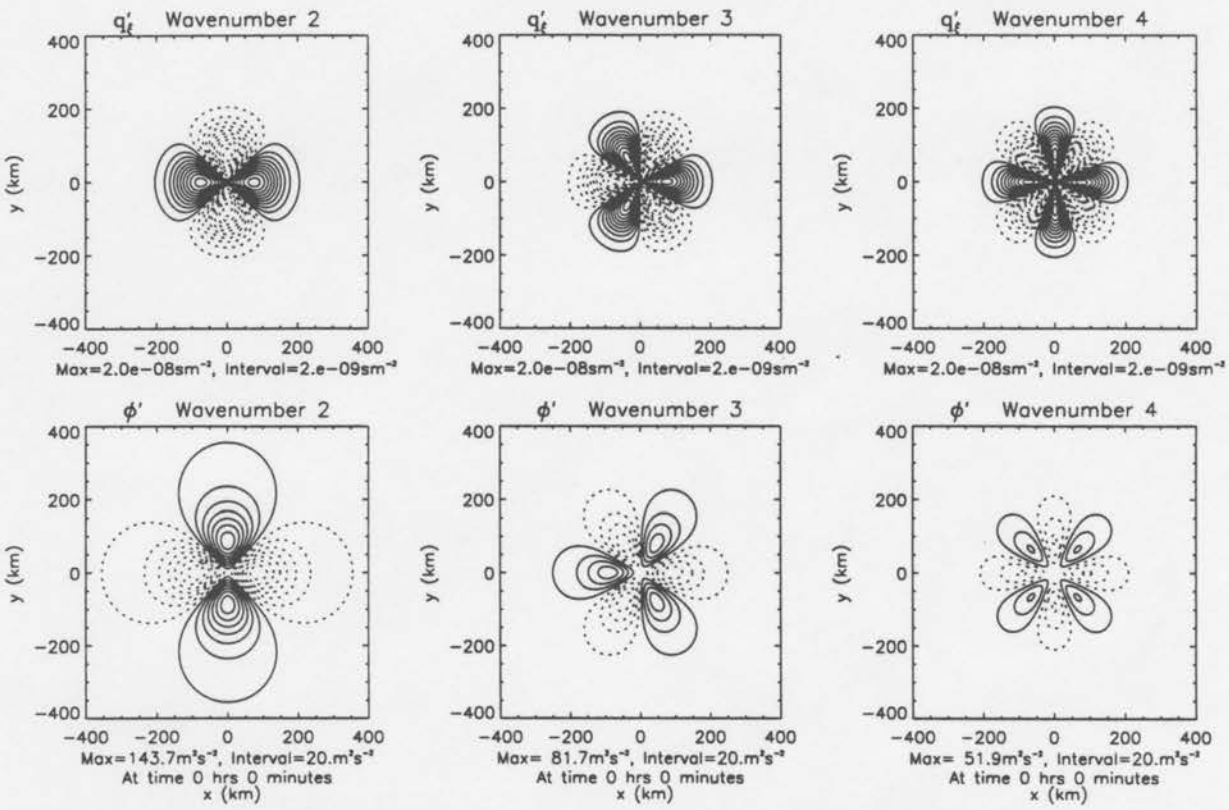

Figure 3.3: Initial q'_ξ, and calculated ϕ' for wavenumbers two, three, and four. All wavenumbers are initialized with the same radial initial condition. Note the decreasing response in ϕ' with increasing wavenumber.

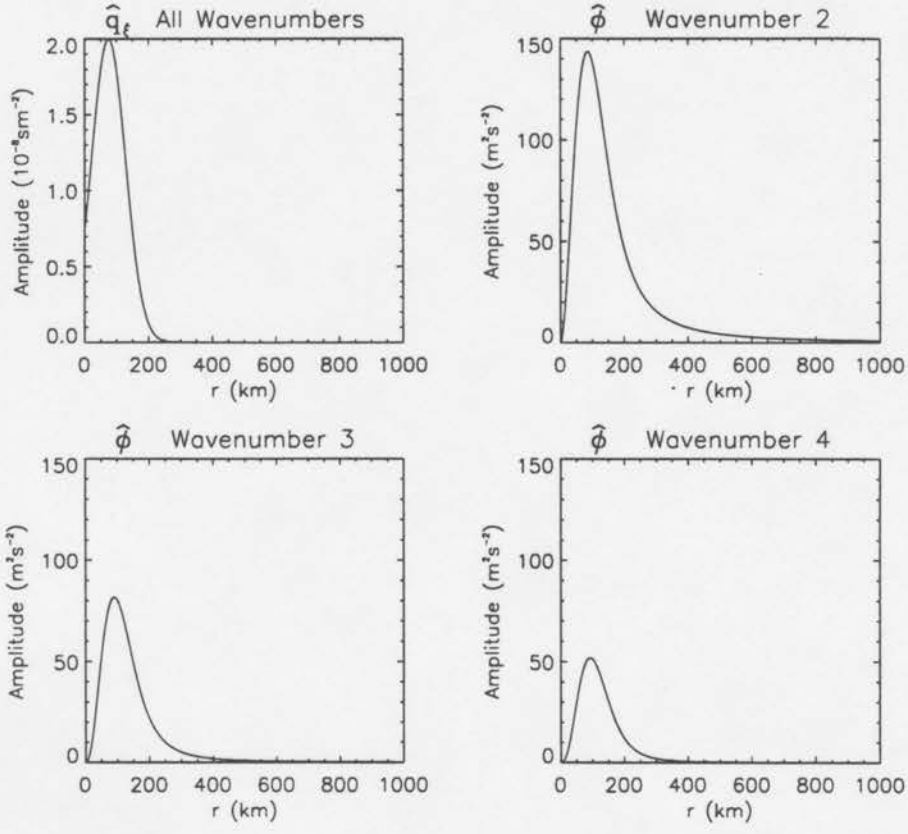

Figure 3.4: Radial profiles of initial $|\hat{q}_\xi|$ (same for all wavenumbers), and calculated $\left|\hat{\phi}\right|$ for wavenumbers two through four. Again note the decreasing $\left|\hat{\phi}\right|$ with increasing wavenumber.

AB model has demonstrated the robustness of the symmetrization process to differing strengths of horizontal diffusion. The robustness of asymmetric decay is in accord with analytical work that conclusively shows the inviscid nature of the symmetrization process (GSM; Carr and Williams 1989; Melander et al. 1987). In particular, GSM provide concise, quantifiable results with which to make comparisons.

3.3.1 Model Comparison

Because the initial asymmetries have significant amplitude where R_n^2 is maximum, this is perhaps the harshest consistency test of the linear AB model for high wavenumbers. Since wavenumber one is zero for the simulations of this chapter, the vortex will remain stationary in the linear f–plane formulation.

GSM examined solutions of the non-divergent, vorticity equation in cylindrical coordinates, linearized on a circular vortex in gradient wind balance. Defining a perturbation streamfunction, ψ, that satisfies continuity,

$$u = -\frac{\partial \psi}{r \partial \lambda} \qquad v = \frac{\partial \psi}{\partial r}, \tag{3.7}$$

the nondivergent vorticity equation can be expressed as,

$$\left(\frac{\partial}{\partial t} + \frac{\bar{v}}{r}\frac{\partial}{\partial \lambda}\right) \underbrace{\nabla^2 \psi}_{\zeta} - \frac{1}{r}\frac{d\bar{\eta}}{dr}\frac{\partial \psi}{\partial \lambda} = 0. \tag{3.8}$$

The vorticity equation (3.8) may be nondimensionalized by defining $r = (RMW)\tilde{r}$; $(u, \bar{v}) = V_{\max}(\tilde{u}, \tilde{v})$; $t = (RMW/V_{\max})\tilde{t}$; $(\zeta, \bar{\eta}) = (V_{\max}/RMW)(\tilde{\zeta}, \tilde{\eta})$; and $\lambda = \tilde{\lambda}$ where tildes denote dimensionless quantities.

In the search for useful analytical solutions, GSM formulated two models: The bounded and unbounded Rankine vortex. The bounded Rankine vortex model had a boundary at the RMW and ten times this radius (CW), $r = a$ and $r = b$ respectively. The basic state wind is irrotational, consequently, the bounded Rankine vortex has no basic state vorticity gradient. The Fourier–Laplace transform of (3.8) is then easily inverted to give

$$\left[\frac{1}{r}\frac{\partial}{\partial r}\left(r\frac{\partial}{\partial r}\right) - \frac{n^2}{r^2}\right]\hat{\psi} = \hat{\zeta}(t) = r\hat{\zeta}_o e^{(-iant/r^2)}. \tag{3.9}$$

The Green's function method yields an explicit solution for the stream function,

$$\hat{\psi}_n(r,\lambda,t) = e^{in\lambda} \int_a^b G(r,\rho)\hat{\zeta}_o e^{(-iant/\rho^2)}\, \rho d\rho, \tag{3.10}$$

where the Green's function is defined as,

$$G(r,\rho) = \frac{1}{2nr^n(a^{2n}-b^{2n})} \begin{cases} (\rho^n - b^{2n}\rho^{-n})(a^{2n}-r^{2n}), & a \le r \le \rho \\ (\rho^n - a^{2n}\rho^{-n})(b^{2n}-r^{2n}), & \rho \le r \le b. \end{cases} \tag{3.11}$$

Vorticity and streamfunction fields for the bounded Rankine model are shown in figures 3.5 and 3.7.

The second of the analytical models, the unbounded Rankine vortex, differs from the unbounded model by including a uniformly rotating core inside $r = a$. In the unbounded vortex the basic state vorticity gradient is confined solely to the RMW where it is infinite. During symmetrization, vorticity anomalies induced by radial flow are confined to the RMW. Because of the singularity in the disturbance vorticity associated with the Rossby edge wave at $r = a$, only streamfunction fields are shown for the unbounded Rankine model. Further discussion on the nature of the unbounded solution is reserved for section 4.3.

In contrast to the above models, the AB model possesses a non–trivial but finite basic state PV gradient throughout the vortex with the maximum occurring inside the RMW. The region that rotates as a solid body collapses to a single point, $r = 0$. Thus, inside the RMW the basic state rotation rate decreases faster than the unbounded Rankine profile. Outside the RMW, on the other hand, the rotation rate falls off more slowly than the Rankine profile.

The first column of figure 3.5 shows the initial perturbations of the GSM and AB models are similar.

3.3.2 Map Plots of Decaying Asymmetries

GSM showed the decay rate of asymmetries in a swirling flow is inversely proportional to the effective shear, $S_{\text{eff}} = r d\bar{\Omega}/dr$. We therefore expect the Rankine profile to symmetrize faster than the benchmark vortex outside the RMW.

Figure 3.5 compares vorticity to PV; and figures 3.7 and 3.6 compare geopotential to streamfunction in the AB and nondivergent models, respectively. Results shown are for wavenumbers two and three. Higher wavenumbers ($n > 3$) evolve similarly and are not shown.

Figure 3.5 compares symmetrization in the GSM and AB models using initially upright vorticity/PV disturbances for wavenumbers two and three whose amplitude is maximum at the radius of maximum winds. The first two rows represent wavenumber two and wavenumber three runs for the GSM model. The last two rows represent wavenumber two and wavenumber three runs for the AB model. Columns correspond to roughly 0, 1/2, and 1 circulation times in both models. The horizontal domain corresponds to four RMW units in both models. It is evident symmetrization in the AB model is very similar to the GSM model. The most noteworthy difference is the fine structure which develops in the near–core region of the AB model. Because the AB model has a basic state PV gradient, radial flow across this gradient creates PV anomalies. This effect diminishes with increasing wavenumber. The significance of this process is further explored in section 3.4.

The variable deformation radius of the AB model complicates the comparison between the streamfunction fields of the GSM model, figure 3.7, and the geopotential fields of the AB model, figure 3.6. The complication arises from the fact that the geopotential is not the streamfunction for the AB wind field. The varying deformation radius partitions the PV disturbance between the flow field and the mass field, smoothing the resulting geopotential field. Keeping these considerations in mind, the comparison nonetheless reveals a qualitative similarity.

GSM provide streamfunction plots for both the bounded and unbounded models, figure 3.7. While the bounded model exhibits long streamfunction filaments near the inner boundary, the unbounded model has a more complicated pattern in the inner–core. This results from radial flow across the basic state vorticity discontinuity at the RMW creating Rossby edge waves. The edge wave then induces a streamfunction response straddling the RMW. The streamfunction response in the solid body rotation portion of the vortex lies in a region of zero effective shear and consequently can never symmetrize. In contrast,

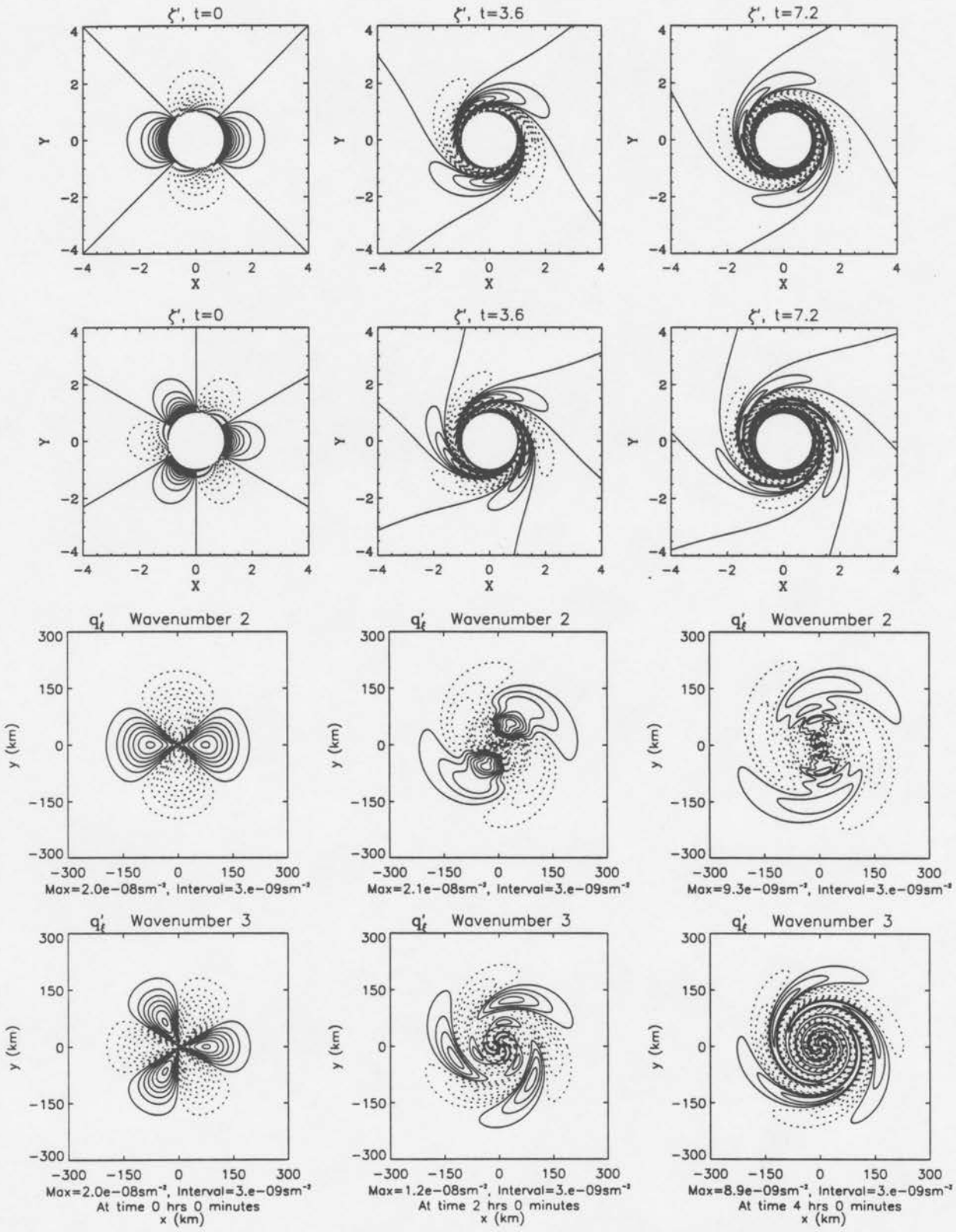

Figure 3.5: Perturbation vorticity, ζ', in the GSM model for the bounded vortex using a contour interval of 6.90×10^{-2} (first two rows). The perturbation potential vorticity, q'_ξ, in the AB model (last two rows). Columns correspond to roughly 0, 1/2, and 1 circulation times in both models. The horizontal domain corresponds to four RMW units in both models.

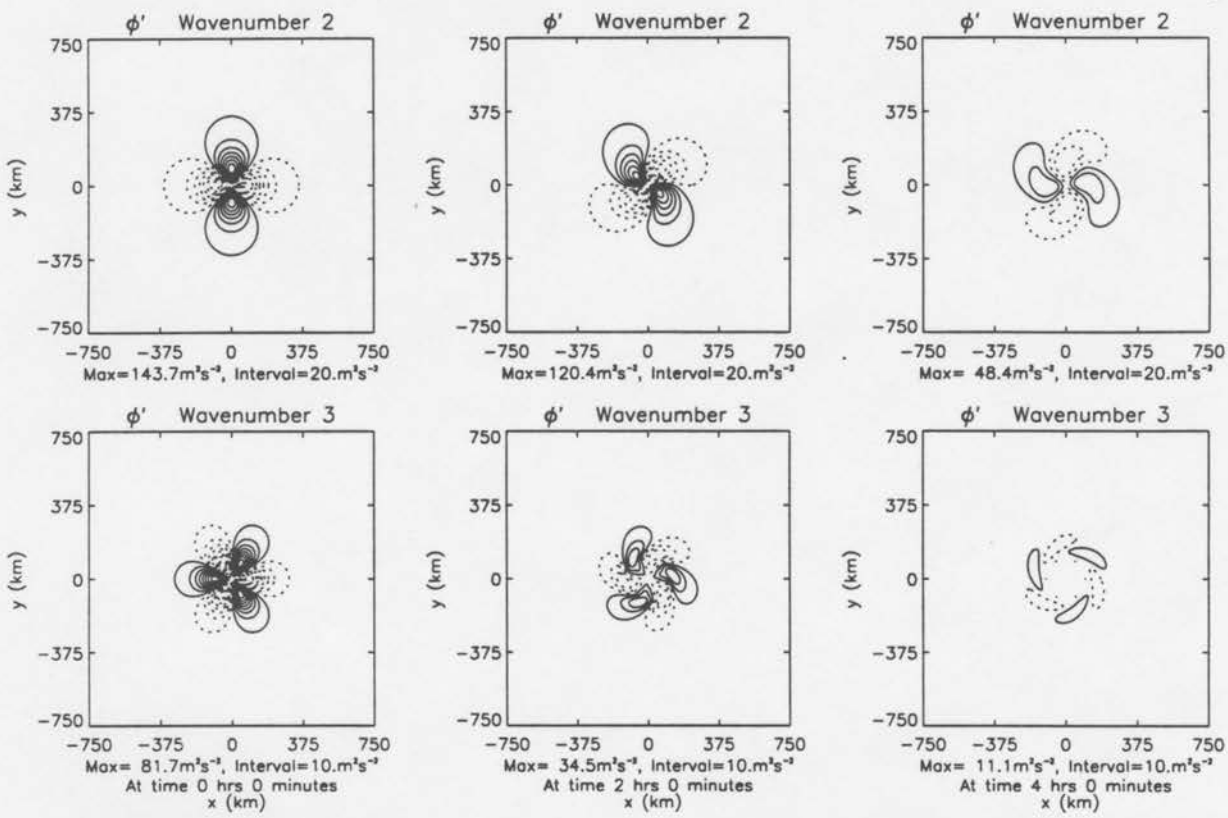

Figure 3.6: Perturbation geopotential in the AB model. The initial asymmetry was maximum at $r = 75\ km$. Note the contour interval difference between $n = 2$ and $n = 3$. The horizontal scale shown is 10 RMW units.

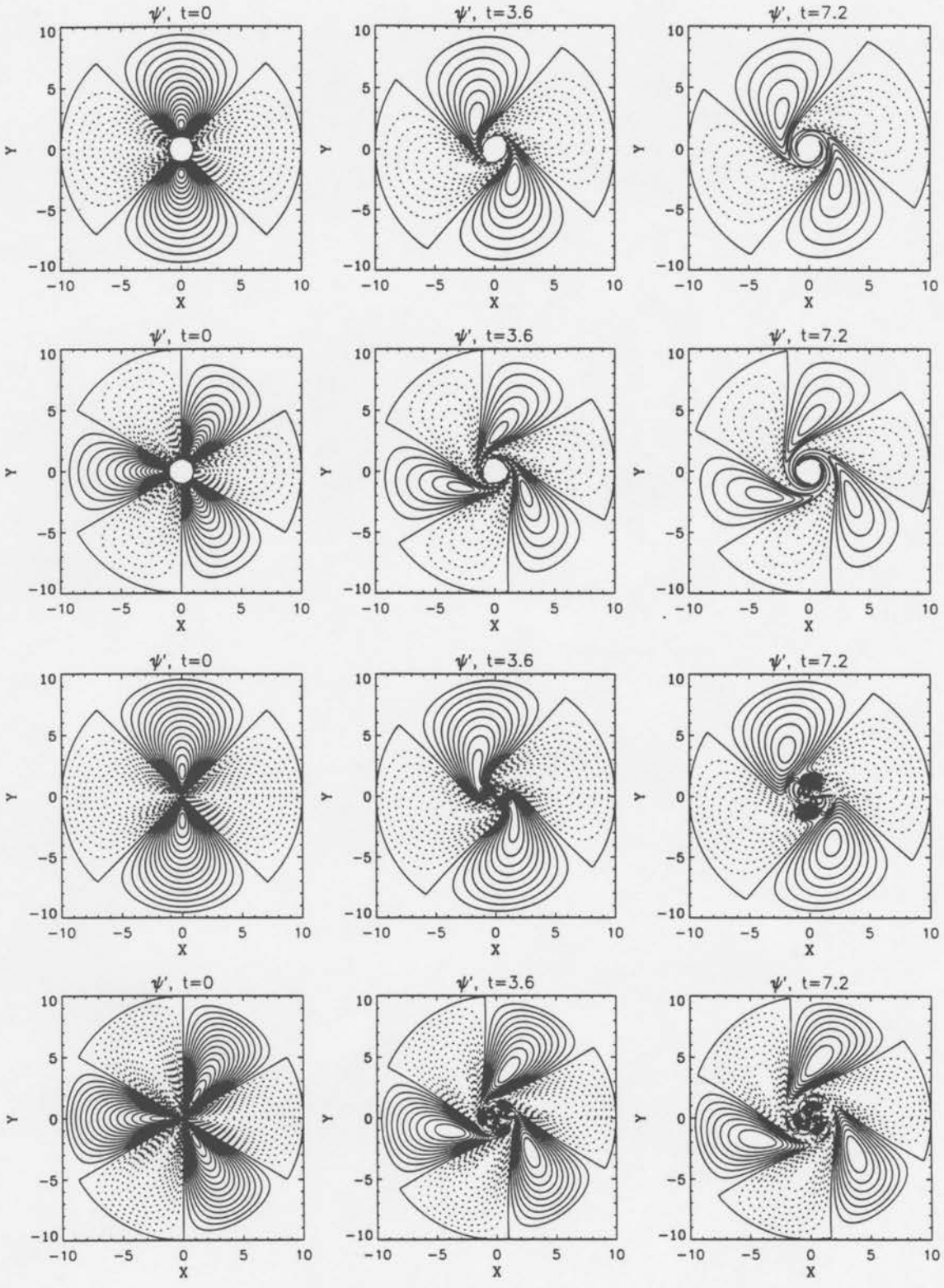

Figure 3.7: Perturbation streamfunction in the GSM model for the bounded (top two rows) and unbounded (bottom two rows) vortex for wavenumbers two and three. For $n = 2$ the contour interval is 5.67×10^{-3}. For $n = 3$ the contour interval is 3.31×10^{-3}. Columns correspond to roughly 0, 1/2, and 1 circulation times. Note the fine scale in the inner–core for the unbounded vortex.

asymmetries outside the RMW will symmetrize. The plots of ϕ' at $t = 2\ hrs$ (figure 3.6) and ψ' at $t = 3.6$ in the unbounded model show the same amount of downshear tilt of the asymmetry.

These comparisons are encouraging testimony in the AB model's ability to correctly represent the symmetrization process at high wavenumbers. To complete the comparison, a more quantitative measurement is desired.

3.3.3 Integrated Energy Decay

When the normalized integrated energy is evaluated for the near–core initial conditions, all asymmetries are observed to decay to roughly 10% of their initial energy after approximately 5 hours ($\approx$ 2 circulation times). Moreover, the decay rate increases with wavenumber and eventually asymptotes. To better understand this behavior, we recall what was learned in the nondivergent model.

Utilizing a Green's function method, GSM derived explicit solutions for integrated energy in linearized nondivergent inviscid vorticity dynamics. In the limit of large azimuthal wavenumbers the integrated energy decay approaches the decay for an unbounded plane wave in rectilinear simple shear:

$$\frac{E}{E_o} = \frac{1}{1 + (S_{\text{eff}}\, t)^2}. \tag{3.12}$$

GSM suggested a plausible candidate for the effective shear, S_{eff}, which would define the limiting energy decay rate as $n \to \infty$ for the Rankine vortex. For the AB model, the GSM expression for S_{eff} is,

$$S_{\text{eff}} = \frac{\int_0^\infty r \frac{d\bar{\Omega}}{dr} \hat{q}_\xi(r)\, dr}{\int_0^\infty \hat{q}_\xi(r)\, dr}, \tag{3.13}$$

and evaluates to, $-3.67 \times 10^{-4} s^{-1}$. This compares to the dimensionalized effective shear calculation used by GSM in the lower panel of figure 3.8 of $-4.98 \times 10^{-4} s^{-1}$. From figure 3.9 we see the limiting decay rate for the Rankine vortex is faster than that of the benchmark vortex used in the AB model. An exception occurs where the normalized energy plots cross the limiting decay curve at around 4.5 hrs. This may be explained

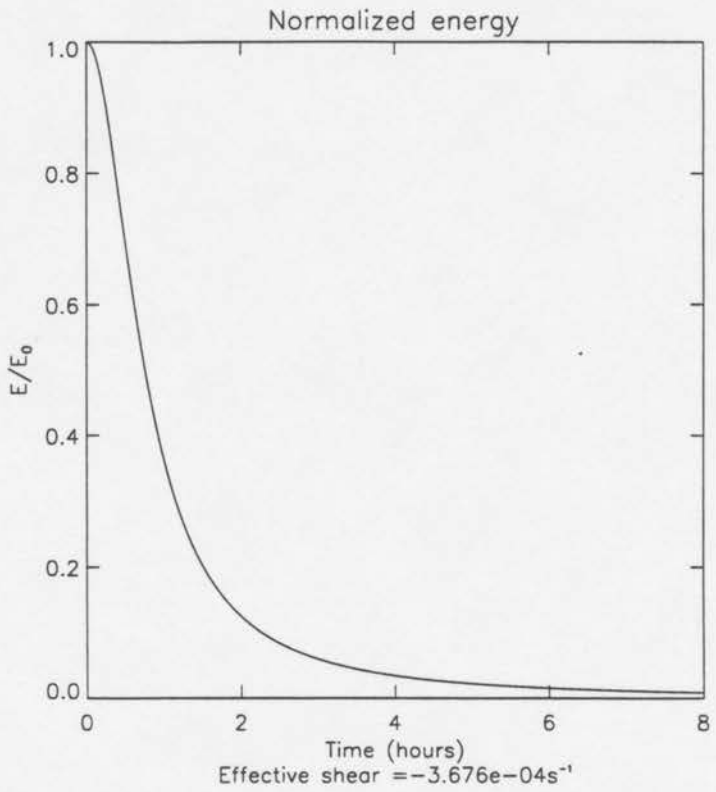

Figure 3.9: Limiting energy decay calculated from the effective shear for the AB benchmark vortex. Comparison with asymmetric decay in the AB model suggests this is the limiting decay as $n \to \infty$.

by the finite deformation radius of the AB model. As the symmetrization proceeds, the radial scale gets very small and the finite influence scale rapidly smoothes these small scales resulting in reduced energy. The demonstration that asymmetric decay in the AB model asymptotes to the limiting decay curve confirms the speculation that AB symmetrization proceeds nearly inviscidly.

Direct comparison between the two models for wavenumbers two and three is made in figure 3.8. The comparison shows good qualitative agreement between the two models with two notable differences. The first of these differences is the decay in the AB model exceeds the decay in the GSM model after about 3 hrs. As noted above, the faster decay rate of the divergent AB model over that of the non–divergent GSM model at long times is attributed to the finite deformation radius which smoothes out short wavelength radial fluctuations. The second difference is the very slow decay rate of wavenumber two in the AB model at short times. CW speculate the symmetrization process would be delayed in a vortex with a basic state vorticity gradient due to differential wave retrogression from an equivalent "β effect" in analogy to the behavior of sheared disturbances in Couette flow on a β–plane. Detailed examination of the evolution of wavenumber two, however, suggests this is not the cause for the delayed decay. The cause is radial flow giving an effective upshear tilt to the asymmetry discussed more thoroughly in section 3.4. The region and magnitude of growth is radially confined delaying the asymmetric energy decay.

3.4 Outer–Core Symmetrization and More

3.4.1 Initialization

As in section 3.2.2 the initial disturbances have Gaussian radial structure in $\hat{q}_\xi$. Wavenumbers two through seven are again considered using $r_{\text{peak}} = 200\ km$ and $r_{\text{fold}} = 75\ km$.

3.4.2 Integrated Energy

Figure 3.10 suggests the evolution of the outer–core asymmetries is significantly different from the inner–core asymmetries. In particular, wavenumber two grows to 137%

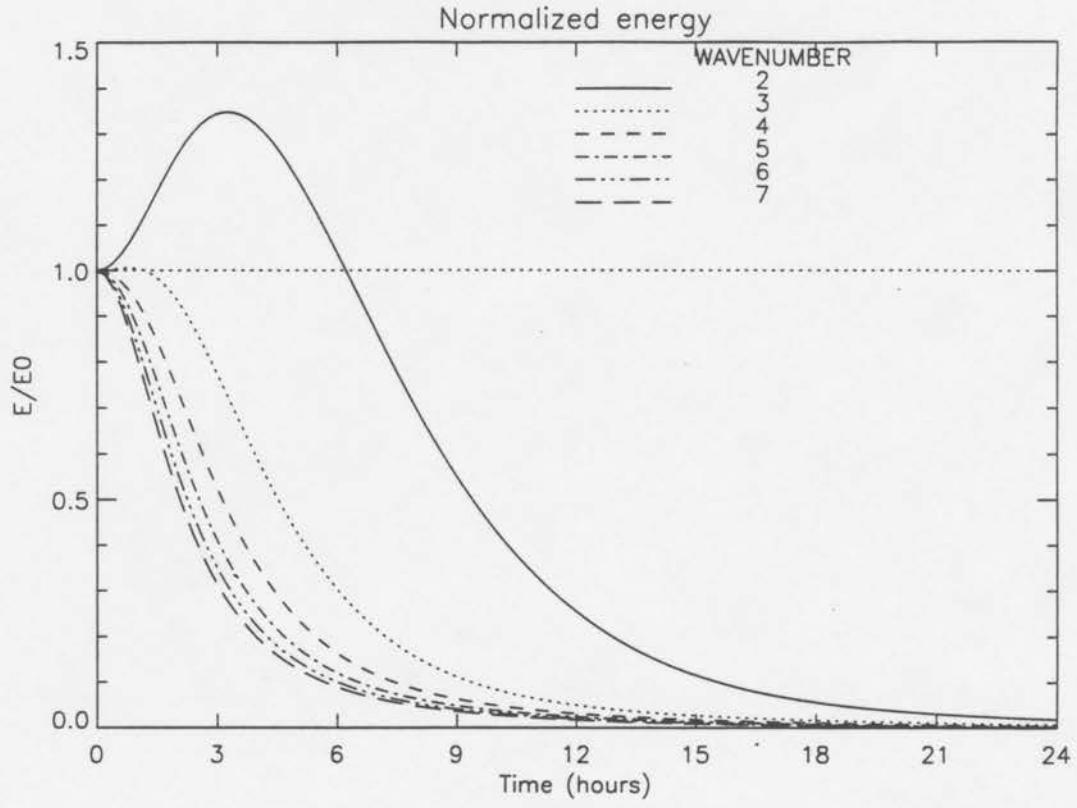

Figure 3.10: Energy decay for an outer–core asymmetry centered at 200 km. Note the slight growth in wavenumber three.

of its initial value in 3 hrs and subsequently decays. Wavenumber three also undergoes a brief growth cycle. Wavenumbers four through seven decay monotonically and behave similarly to the inner–core case. One might assume the growth is a result of the diverging series expansion used to derive the AB model. However, the growth pattern of figure 3.10 is not consistent with this assumption. First, if the growth were the result of the expansion parameter being large, one would suspect that the highest wavenumbers would grow the most. Secondly, to further examine the nature of the growth, we put the initial asymmetries at 1500 km, in the QG regime. This region was chosen because both local and environmental Rossby numbers are < 1 for wavenumbers two through seven. Therefore, if the growth is a result of the diverging series solution, these asymmetries should monotonically decay. Instead, wavenumbers two and three grew more than they did at 200 km and wavenumber four grew slightly as well. Not surprisingly, the asymmetries evolved very slowly in response to low shear at that region with the growth/decay cycle

taking much longer than the case at 200 km. To better understand the physics of the observed growth, we now examine three fields of the growing wavenumber two asymmetry initialized at 200 km.

3.4.3 Origin of the Transient Growth

To elucidate the growth process observed in subsection 3.4.2, the evolution of wavenumber two is examined more closely. Figure 3.12 is a time series showing three fields; perturbation potential vorticity, perturbation geopotential, and Reynolds stress. The results are shown for three times: initially, at the start of the growth cycle, and during the decay cycle. Of the three fields shown, the Reynolds stress field warrants more discussion.

Recall the formulation of the analogous Reynolds stress term and its relation to disturbance energy tendency. Equation (2.36) shows the change in disturbance energy at a point has three contributions; advection by the basic state, work done by pressure forces, and the Reynolds stress times the product of the column height and the effective shear. Integrating over the entire domain eliminates the first two contributions. It will prove useful, therefore, to investigate the spatial distribution of the Reynolds stress in order to identify regions of the vortex which might favor growth or decay. Figure 3.11 is a plot of the basic state portion of the Reynolds stress growth term including the minus sign and metric factor r, $-\frac{\bar{\Phi}}{g} r^2 \frac{d\bar{\Omega}}{dr}$. This function may be interpreted as indicating the most favored location for energy exchange with the basic state. The radius where the benchmark vortex is most susceptible to interactions with disturbances by the Reynolds stress is outside the RMW at 130 km. The potential for interaction quickly falls to zero in the inner–core and falls to 25% of peak value by 1000 km. This basic state quantity then multiplies $u'_\eta v'_\xi$ to get the Reynolds stress contribution to the asymmetry energy tendency. The quantity $u'_\eta v'_\xi$ is positive when the asymmetry fluxes cyclonic momentum out of the vortex or anticyclonic momentum into the vortex. For an everywhere positive $-\frac{\bar{\Phi}}{g} r^2 \frac{d\bar{\Omega}}{dr}$, the asymmetry grows. The quantity $u'_\eta v'_\xi$ is negative when the asymmetry fluxes cyclonic momentum into the vortex or anticyclonic momentum out of the vortex resulting in asymmetry decay.

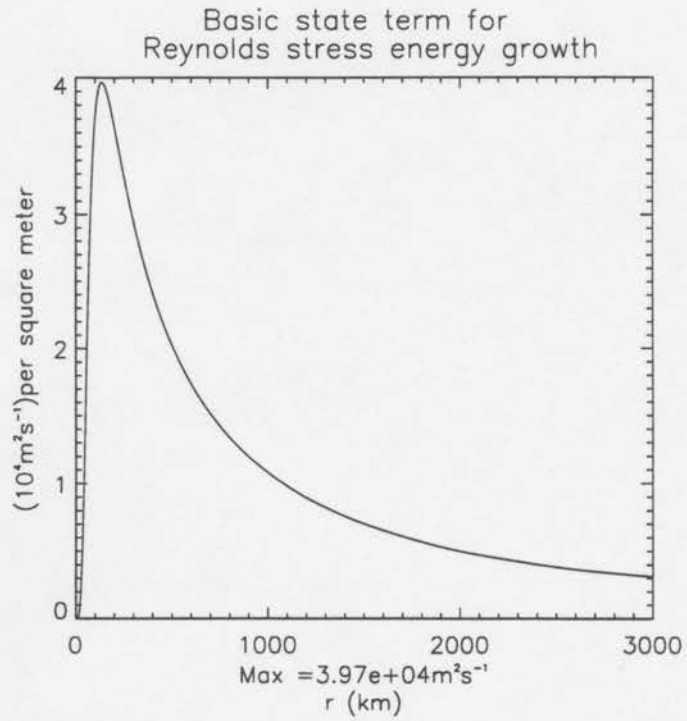

Figure 3.11: Basic state contribution, including the metric factor r, to energy growth from Reynolds stress, $-\frac{\bar{\Phi}}{g} r^2 \frac{d\bar{\Omega}}{dr}$.

The first column of figure 3.12 are the initial wavenumber two fields. The PV disturbance induces the geopotential disturbance of the second row. The disturbance geopotential then has an associated balanced wind but initially the Reynolds stress gives no net asymmetry decay or growth. This has been confirmed by integrating the Reynolds stress field around any radial circle and finding it to be zero. This benign pattern will rapidly change in response to the deformation flow associated with the initial asymmetry.

After 1 hr the radial flow has forced PV anomalies near 60 km, the radius where the gradient of the basic state PV is maximum. The invertibility relationship then produces a geopotential response possessing an upshear tilt (cf. Farrell 1982; also Boyd 1983). The upshear tilt is limited to approximately half of an azimuthal wavelength. This limits the degree of upshear tilt and the amount of algebraic growth which can be realized from an initially upright asymmetry. The Reynolds stress contribution to the energy tendency shows net growth at $r = 130$ km and is maximum near the zero value contour of the geopotential field. Also noteworthy in the Reynolds stress plots is the fact that outside

of 200 km, there is still no net growth/decay. This is consistent with the fact that the geopotential has changed only slightly from the initial condition.

In contrast to the plots at $t = 1\ hr$, the plots for $t = 6\ hrs$ show a decaying asymmetry. The inner–core asymmetry has rotated 135° while the outer asymmetry has rotated less than 90°. The differential rotation has reversed the upshear tilt to a downshear tilt. The fine structure of the disturbance PV field is the result of the inner–core response to quasi–steady forcing from the slowly decaying outer asymmetry. In terms of the Reynolds stress, the decay occurs at two distinct radial locations. Higher time resolution plots reveal the nature of the two decay regimes. The decay maximum at 260 km corresponds to the decaying initial asymmetry. The other maximum occurs at 200 km coinciding with the radius that separates the inner and outer asymmetries of the disturbance PV at $t = 6\ hrs$.

The azimuthal motion of the PV asymmetries differs from that of the storm's rotation rate. Experience has shown that the azimuthal motion is a complex function of n, the radial scale, the basic state PV profile, and the basic state tangential wind profile. Examination of the parameter space for the azimuthal group velocity derived in chapter 5 reveals an effect which changes the evolution of the upshear/downshear tilt geometry. Relative to the basic state, the azimuthal group velocity tends to have the largest positive values in the inner–core and near–core and has small positive or even negative values at larger radii. This difference becomes more significant with increasing wavenumber. This effect accelerates the reversal from upshear to downshear tilt, further limiting the potential for algebraic growth of high wavenumber asymmetries.

3.5 Summary

In this chapter the AB model has been validated for high wavenumber asymmetries on a stable vortex, specifically wavenumbers two through seven. Despite the formal divergence of the asymptotic series, the zeroth–order truncation accurately evolves high wavenumbers.

The AB model was validated with a side–by–side comparison using bounded and unbounded analytical models for nondivergent vorticity dynamics. Dynamical quantities showed excellent agreement between the AB and GSM models. The limiting decay as

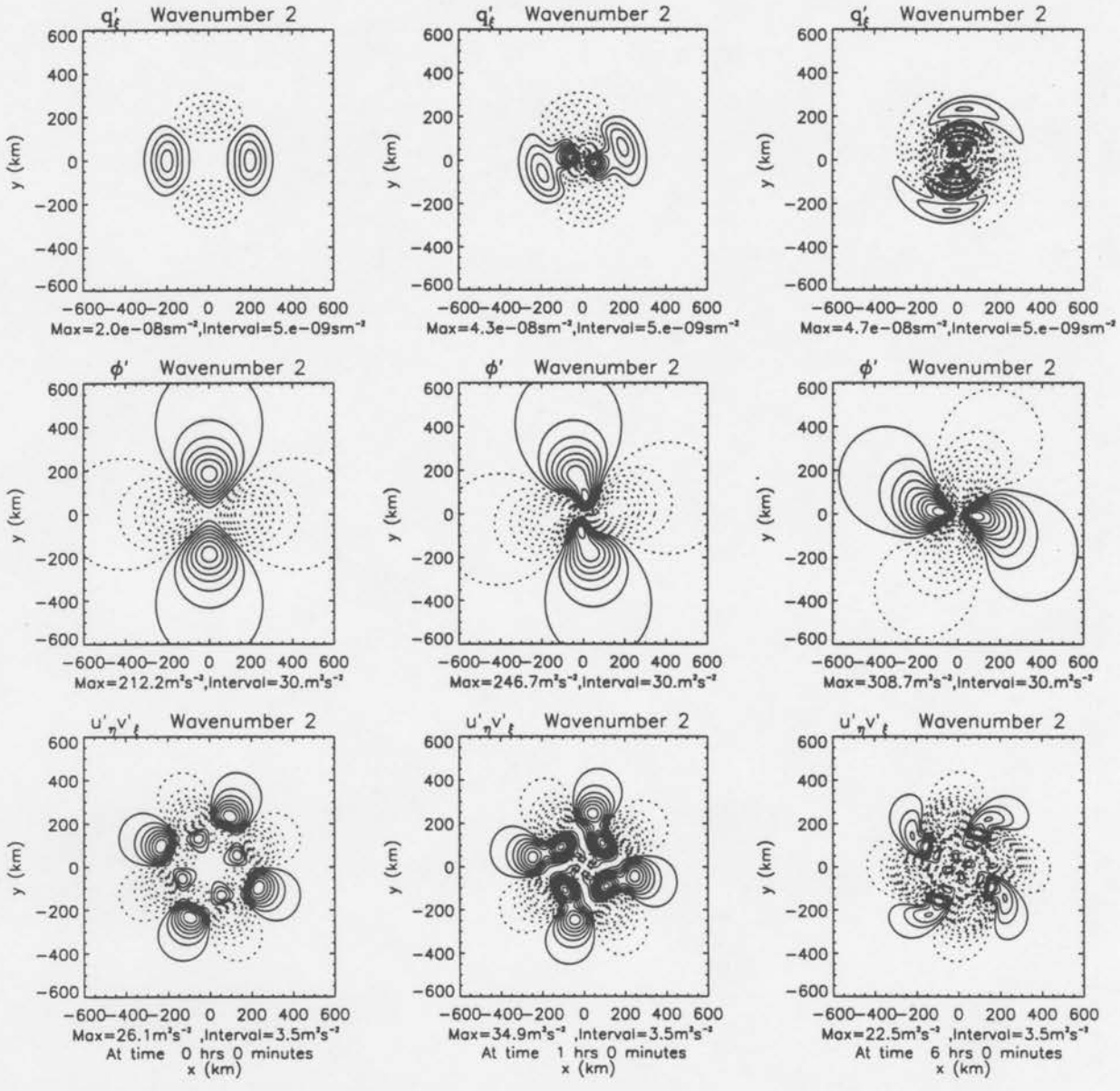

Figure 3.12: Map plots of q'_ξ, ϕ', and Reynolds stress $(u'_\eta v'_\xi)$ for wavenumber two showing transient growth for an outer–core asymmetry.

determined by the effective shear predicts the limiting decay as $n \rightarrow \infty$ for the AB model. Most of the differences between the two models can be traced to the variable deformation radius and the smoothly changing basic state PV gradient of the AB model. The variable deformation radius accelerates the energy decay by smoothing the small radial scales that occur during the symmetrization process. Radial flow across the basic state PV gradient produces small scale PV anomalies in the inner–core of the vortex. While an analogous effect also occurs in the unbounded nondivergent analytical model in the form of Rossby edge waves, this response is limited to just one vorticity anomaly in the radial direction.

The AB model exhibited algebraic growth for some outer–core asymmetries. The growth cycle starts with radial flow from the initially upright asymmetry inducing PV anomalies in the inner–core where the basic state PV gradient is large. The invertibility relationship provides a positive Reynolds stress resulting in upshear tilt and algebraic growth. The n^2 dependence in the invertibility relationship greatly limits this sequence of events at higher wavenumbers. Algebraic growth is also observed with inner–core asymmetries but the effect is greatly reduced because of the smaller influence scale. This effect merely serves to hold off the decay of wavenumber two for a short while.

Chapter 4

WAVENUMBER ONE

4.1 Introduction

Observations show that wavenumber one is the dominant asymmetry in mature hurricanes (SM). Although the series solution in the AB formulation for wavenumber one should converge for hurricane–like vortices, it is of great practical interest to examine the evolution of wavenumber one in the AB model. As we shall see, this exercise also elucidates the unique physics of wavenumber one.

Although it has been discussed elsewhere, it is useful to summarize the various environmental factors that force wavenumber one asymmetries in a hurricane. From a Taylor series expansion about the grid center, Willoughby (1992) shows both the environmental flow at the center and the environmental vorticity gradient across the vortex project onto wavenumber one. Often the largest contribution from the environmental vorticity gradient is the planetary vorticity gradient giving rise to the so–called "β gyres" (Franklin et al. 1993). Frictional stress under a moving storm produces wavenumber one forcing (Shapiro 1983). A tilting of the vortex by vertical shear also results in wavenumber one forcing. Eyewall convection is often observed to have a wavenumber one component, especially in the vortex development stage. These are just a few of the various asymmetric forcings that act on a hurricane during its life cycle. As a first step towards understanding the evolution of wavenumber one asymmetries that are continuously forced, this work assumes a quiescent environment at the boundaries and examines the evolution of asymmetric conditions from the perspective of an initial value problem.

In the polar representation, using azimuthal Fourier modes, Willoughby(1992) uses a Taylor series representation to show small differences between the vortex center and the

grid center project primarily onto wavenumber one. He refers to this contribution as the "alpha gyre" and developed a procedure called "alpha gyre closure" for selecting a new grid center that minimizes the energy of wavenumber one. The capability of selecting a new grid center that minimizes the energy of the asymmetries also exists in the current AB model but has not been used. This procedure entails decomposing the total field about the new center and redefining the basic state. Since this could have the undesirable effect of altering the stability properties engineered into the benchmark vortex, we decided to keep the physics as simple as possible. Repositioning the grid center and decomposing the fields azimuthally about that new center can be thought of as a non–linear effect since each of the old wavenumbers may now project onto different wavenumbers. As long as the positioning error is small, however, the resulting contribution to wavenumber one will be small and the linear perturbation assumption will remain valid. For linear dynamics on an f–plane, the AB model will be shown to accurately evolve wavenumber one in a stationary grid.

The benchmark vortex of chapter 3 is initialized with the same Gaussian structure of $\hat{q}_\xi$ used in section 3.2.2 for wavenumber one with $r_{\text{peak}} = 200\ km$, $A_\circ = 2 \times 10^{-9} sm^{-2}$, and $r_{\text{fold}} = 100\ km$.

4.2 Integrated Energy

The integrated energy plot of figure 4.1, shows a marked difference to the decay plots of the higher wavenumber asymmetries of chapter 3, see figures 3.8 and (3.10). Wavenumber one goes through an initial growth cycle as did wavenumber two for the outer–core asymmetry, but the growth is six times larger than the growth in wavenumber two. The growth cycle reverses to decay at 10 hrs whereas in the wavenumber two case this reversal occurred at 3.5 hrs. These differences are easily explained by the n^2 dependence in the invertibility relationship. The large influence scale allows greater cross correlation between the inner and outer asymmetries, discussed in section 4.4. Another contribution to the differences between the growth and decay cycles of wavenumbers one and two is the wavenumber dependence of the azimuthal group velocity discussed in section 5.4.

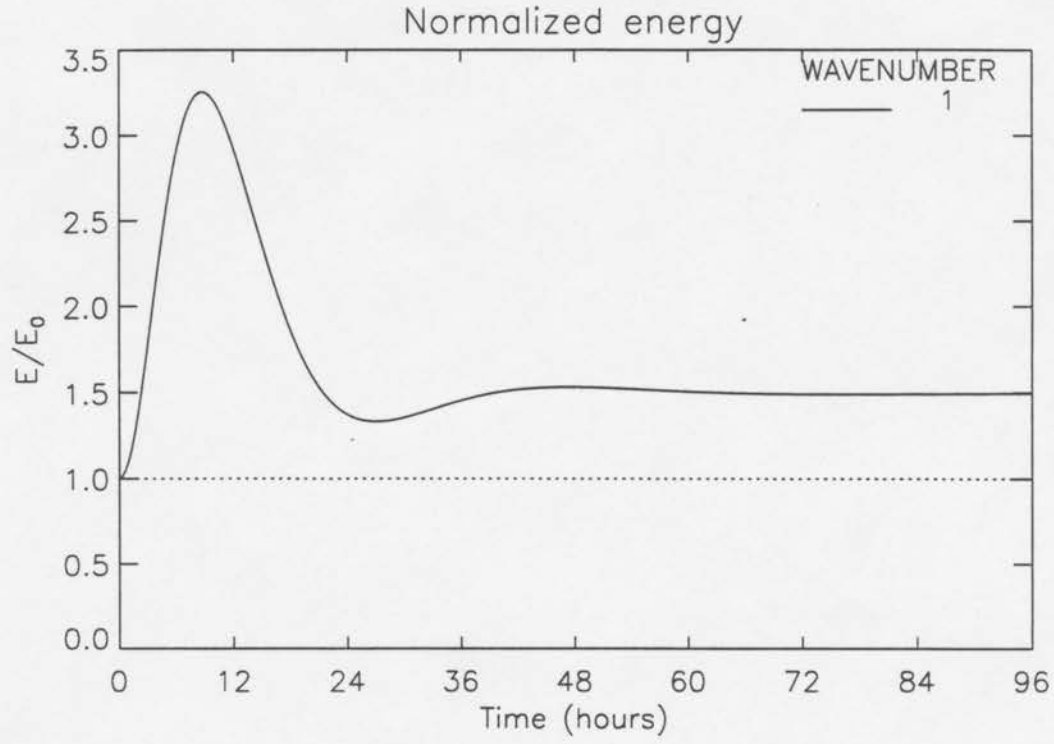

Figure 4.1: Normalized energy curve for an initial wavenumber one asymmetry at $r = 200\ km$. Note how the plot asymptotes to 150%.

The most significant difference between the integrated energy decay of wavenumber one and higher wavenumbers is the value to which the asymmetries decay. All high wavenumber asymmetries decay to zero no matter the initial condition. This is unlike the behavior of wavenumber one which asymptotes to the non–zero value of 150%.

4.3 Long term solution: the Pseudo mode

The non–divergent model is once again very helpful in understanding features observed in the AB model.

By applying matching conditions across the discontinuity in the basic state vorticity, GSM derive the following solution for the Fourier amplitude of the streamfunction in the unbounded Rankine vortex,

$$\hat{\psi} = \int_0^\infty G(r,\rho)\hat{\zeta}_{so} e^{-in\bar{v}t/\rho}\,\rho d\rho - \hat{\Psi}_1 \frac{2n}{a}\int_0^\infty \frac{G(a,\rho)\hat{\zeta}_{so}}{(n-1-an\bar{v}/\rho)} e^{-in\bar{v}t/\rho}\,\rho d\rho$$
$$+\hat{\Psi}_1\left[\gamma_o + \frac{2n}{a}\int_0^\infty \frac{G(a,\rho)\hat{\zeta}_{so}}{(n-1-an\bar{v}/\rho)}\,\rho d\rho\right] e^{-i(n-1)t/a}, \qquad (4.1)$$

where γ_o is the initial amplitude of the Rossby edge wave,

$$\hat{\Psi}_1 = -\frac{a}{2n}\begin{cases} a^{-n}r^n, & 0 \le r \le a \\ a^n r^{-n}, & a \le r < \infty \end{cases},$$

$\hat{\zeta}_{so}$ represents the smooth part of the disturbance vorticity. The Green's function along with other variables are defined in section 3.3.1.

GSM then make the following interpretation. The first line of (4.1) is identified with the continuous spectrum solution and is the unbounded analogue of the bounded solution presented in section 3.3.1. The second line is a conversion term that transfers some of the energy in the continuous spectrum solution into the discrete mode, which is the third line of the equation. Interestingly, even with no edge wave component initially ($\gamma_o = 0$), the continuous spectrum solution always projects onto the edge wave at later times (cf. Farrell, 1984).

For smooth vorticity initial conditions that are zero within the RMW, the oscillating intergal of the first two terms of equation (4.1) will vanish as $t \to \infty$. For $n = 1$, the last

term is a function of r and λ only. In this case, as $t \to \infty$,

$$\hat{\psi}(r) \to \hat{\Psi}_1 \left[\gamma_o + \frac{2n}{a} \int_0^\infty \frac{G(a,\rho)\hat{\zeta}_{so}}{(n-1-an\bar{v}/\rho)} \rho d\rho \right], \tag{4.2}$$

The radial dependence of $\hat{\Psi}(r)$ for $n = 1$ is merely proportional to $\bar{v}(r)$. Thus, the longtime streamfunction for wavenumber one is simply the image of the basic state vortex, the pseudo mode. The continuous nondivergent model behaves similarly yielding the pseudo mode at long times,

$$\hat{\psi}(r) \to -\frac{1}{4} \left[\int_0^\infty \rho^2 \hat{\zeta}_o(\rho) \; d\rho \right] \bar{v}(r) \tag{4.3}$$

The pseudo mode does not rotate and will be shown to predict the new location of the vortex. An important conceptual distinction should be made between alpha gyres and the pseudo mode. An alpha gyre arises from a difference between the grid center and vortex center for whatever reason, whereas the pseudo mode is an alpha gyre forecasted by wavenumber one in a stationary grid model. Adding the pseudo–mode geopotential to the basic–state geopotential predicts a new vortex center 12.5 km to the ESE of the original center. As discussed below, the orientation of the psuedo mode in figure 4.2 is influenced by the outer boundary condition. The steady state nature of the pseudo mode implies the following expression for the wavenumber one wind components,

$$u' = -\frac{1}{\bar{\eta} r} \frac{\partial \phi'}{\partial \lambda} - \frac{\bar{\Omega}}{\bar{\eta}\bar{\xi}} \frac{\partial}{\partial \lambda} \left(\frac{\partial \phi'}{\partial r} \right), \tag{4.4}$$

and

$$v' = \frac{1}{\bar{\xi}} \frac{\partial \phi'}{\partial r} - \frac{\bar{\Omega}}{\bar{\xi}\bar{\eta} r} \frac{\partial^2 \phi'}{\partial \lambda^2}. \tag{4.5}$$

These expressions were evaluated and plotted at $t = 72\ hrs$ in figure 4.2. The maximum $\left|\vec{\mathbf{u}'}\right|$ of $4.7 ms^{-1}$ is from the NNE and located at the origin.

Equation (4.3) not only shows the pseudo mode is steady but it also has the same orientation as the initial asymmetry. For this initial condition it should then have the same radial structure but be oriented with the PV maximum directly east. Figure 4.2, however, shows the pseudo mode is slightly rotated. This effect is believed to be a boundary influence due to the fact that (4.3) is a solution to (4.1) only as $r \to \infty$. For a finite

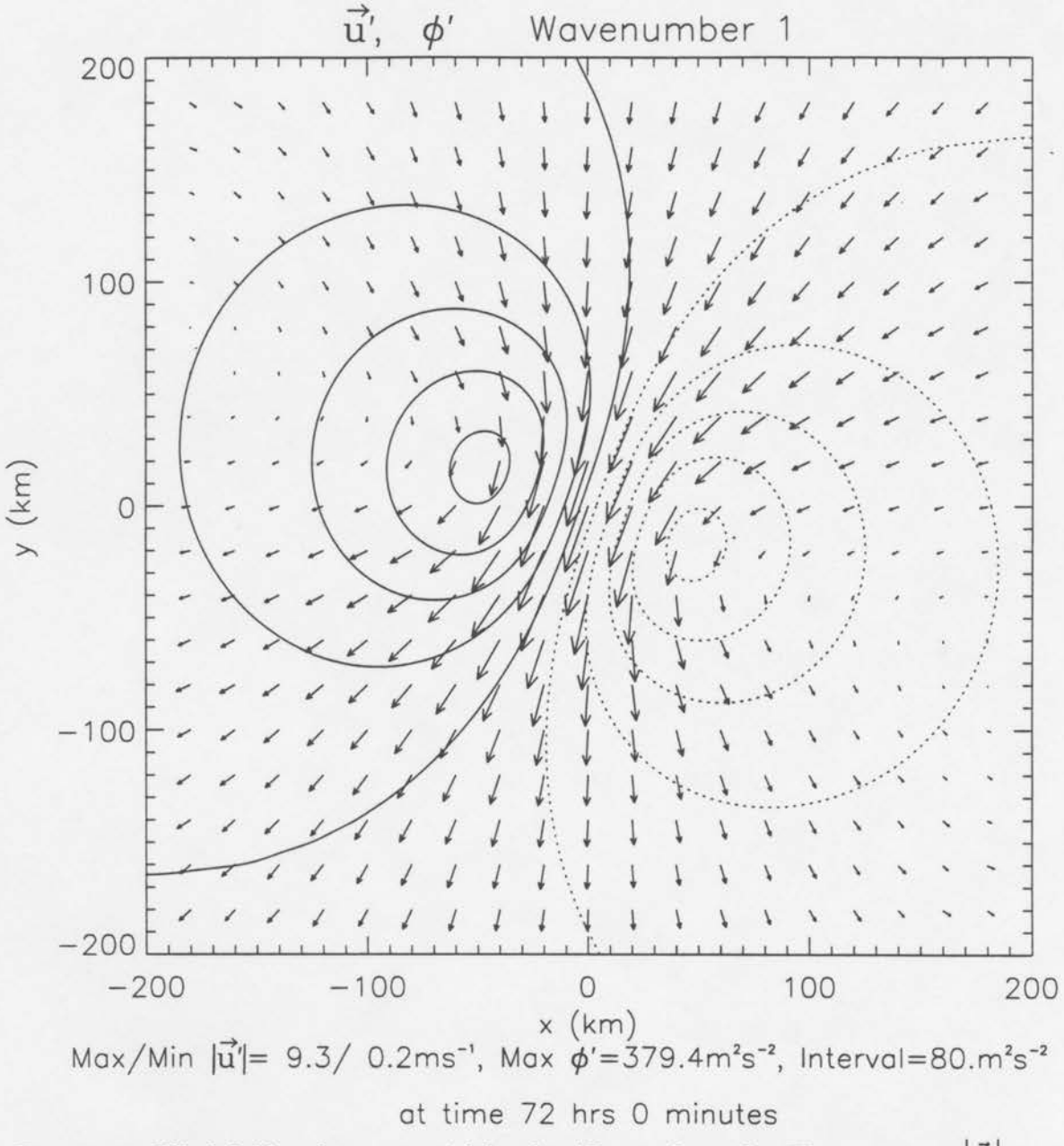

Figure 4.2: Wind field and geopotential for the AB pseudo mode. The maximum $|\vec{u}'|$ is located at the origin. Note the large cross contour flow. Negative contours are dashed. The new vortex center is located 12.5 *km* from the original center in the direction of the low.

outer boundary it can be shown that the magnitude and radial structure are unchanged but a slowly rotating component exists at all times. The finite boundary therefore causes the vortex to slowly rotate about the original center. For the AB simulation discussed here the magnitude and radial structure did indeed remain unchanged and the rotation rate was found to be very small, $1.3 \times 10^{-6} s^{-1}$. The positioning error after 72 hrs was 6 km, twice the radial grid spacing of the numerical model. This error minimally effects vortex motion and only indirectly effects the symmetrizing component through the slowly rotating influence of the pseudo mode. The fact that the boundaries have a small effect on the storm motion is understood by considering the entire fluid domain as the vortex. Every fluid column must move in concert with the vortex center, but the perturbation winds are effectively forced to vanish at the boundaries in the stationary grid. Action at a distance then reaches across the domain causing every fluid column to have a small–amplitude, slowly–rotating component.

4.4 Algebraic Growth: the Transient Response

The first column of figure 4.3 shows the initial wavenumber one fields. The PV disturbance induces the geopotential disturbance of the third row. The disturbance geopotential then has an associated balanced wind but the Reynolds stress shows no net asymmetry decay or growth. This benign pattern rapidly changes in response to the radial flow associated with the initial asymmetry.

The second column is representative of the growth phase. As in the the wavenumber two example of section 3.4.3, radial flow across the basic state PV gradient forces PV anomalies in the inner–core. For the sake of clarity, the PV plots have been partitioned between the first and second rows. The partition was chosen in such a way that the fine scale structure of the symmetrizing portion appears in the first row, while the entire pseudo mode ultimately emerges in the second row. Note the large difference in contour intervals used in the first and second rows. The invertibility relationship produces a response in the geopotential which has an upshear tilt and subsequent algebraic growth. The Reynolds stress contribution to the energy tendency shows net growth at $r = 110$ km. Although

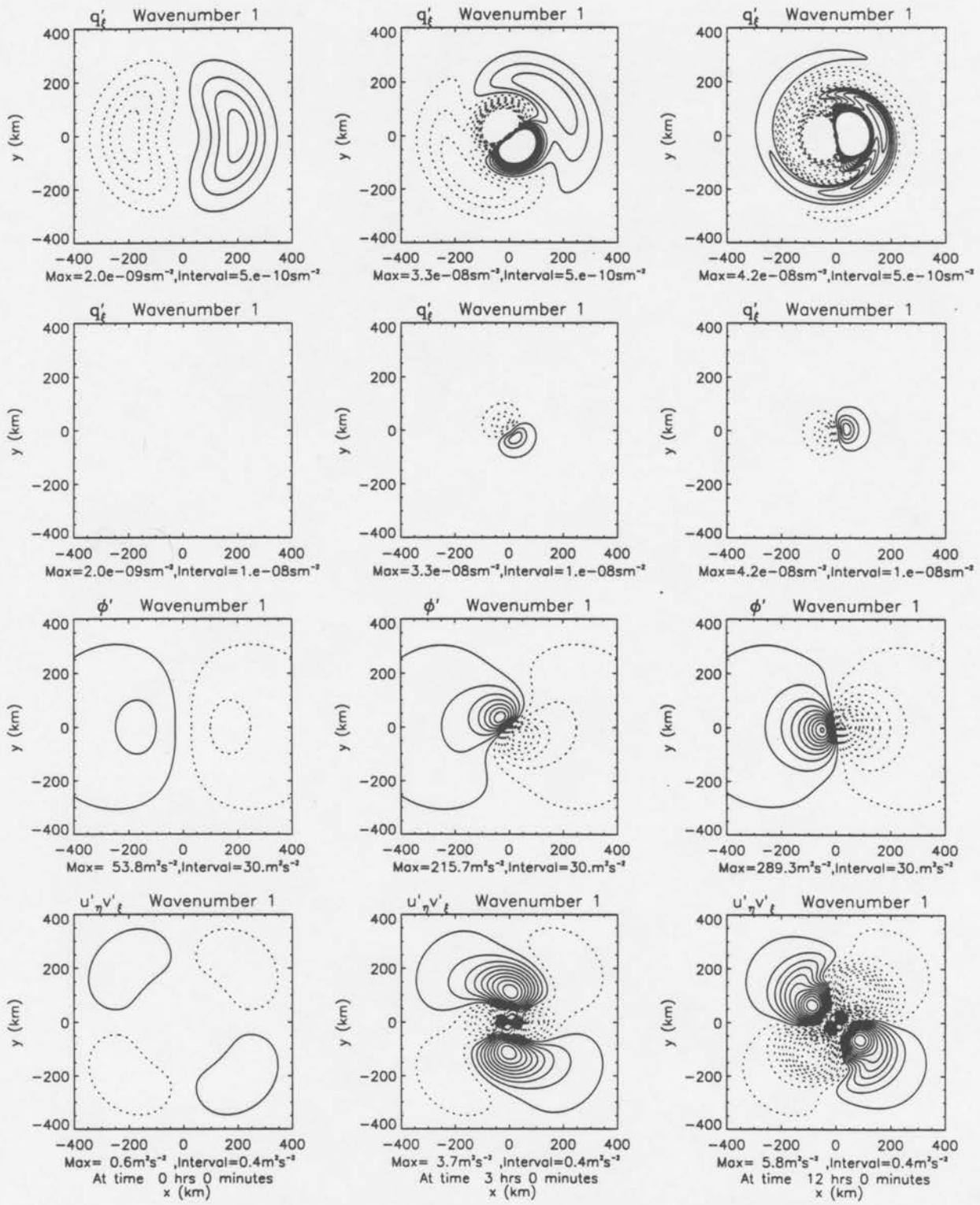

Figure 4.3: Map plots of q'_ξ, ϕ', and Reynolds stress ($u'_\eta v'_\xi$) for wavenumber one showing transient growth and the emerging pseudo mode. For the sake of clarity, the PV plots have been partitioned between the first and second rows. The partition was chosen in such a way that the fine scale structure of the symmetrizing portion appears in the first row and the entire pseudo mode ultimately emerges in the second row. Note the difference between the contour intervals used in the first and second row.

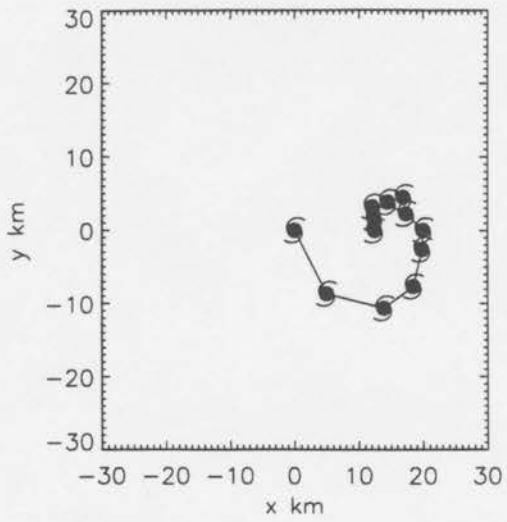

Figure 4.4: Positions of the minimum geopotential every 2 hrs in the AB model. This represents the vortex motion resulting from the initial wavenumber one asymmetry. The initial condition employs the Gaussian profile used throughout this chapter at twice the amplitude ($A_o = 4 \times 10^{-9} sm^{-2}$). The hurricane symbols show storm position every two hours starting with plot #0 for $t = 0$ located at $(x, y) = (0, 0)$. The 11^{th} plot corresponds to both $t = 22\ hrs$ and $t = 24\ hrs$.

the Reynolds stress is large inside the radius $r = 50\ km$, the pattern is nearly symmetric and contributes little to the growth or decay.

The third column is representative of the decay phase. The figures show how the pseudo mode has interfered with the algebraic growth, cf. figure 3.12. The initial asymmetry (row one) has wrapped through 360°. But since the pseudo mode (row two) has such a large value, its influence scale reaches across the trailing arm and results in only a small downshear tilt in the geopotential field. This interference effect combined with the eventually steady–state nature of the pseudo mode greatly prolongs the growth and decay cycle of the transient response.

When viewed from a stationary grid, the wavenumber–one evolution detailed in figure 4.3 can be interpreted as transient vortex motion in response to an initial "push". The "push" is not impulsive nor is it from a constant direction. The initial asymmetry slowly rotates and symmetrizes producing a weakening advective flow across the vortex (cf. Fig. 15a and accompanying discussion of Smith et al. 1990). Since the total geopotential field is nearly circular, the minimum geopotential is a good first guess at the vortex location.

By tracking the minimum geopotential, figure 4.4 shows the transient vortex motion. The hurricane symbol shows the position every two hours starting with plot #0 for $t = 0$ located at $(x, y) = (0, 0)$. The 11^{th} plot is the plot for both $t = 22\ hrs$ and $t = 24\ hrs$. This interpretation clarifies the importance of the pseudo mode. The pseudo mode represents the integrated effect of the initial asymmetry on storm motion including the transient growth/decay cycle.

4.5 An Exact Solution

For azimuthal wavenumber one, equation (3.8) may be integrated exactly (Smith and Rosenbluth 1990). The solution is

$$\hat{\psi}_1(r,t) = -r \int_r^\infty dr'\, e^{-it\bar{\Omega}(r')t} \left[1 + it\bar{\Omega}(r) - it\bar{\Omega}(r')\right] \hat{h}(r'), \tag{4.6}$$

where

$$\hat{h}(r) = \frac{1}{r^3} \int_0^r d\rho\, \rho^2\, \hat{\zeta}^{(0)}(\rho), \tag{4.7}$$

and $\hat{\zeta}^{(0)}$ denotes the initial radial structure of relative vorticity for wavenumber one. The derivation of (4.6) exploits the fact that $\hat{\psi}_1(r,t) = r\bar{\Omega}(r)$ (the pseudo-mode) is an exact, steady solution of (3.8). The resulting second-order radial structure equation in Fourier-Laplace space can be reduced to a first-order equation and integrated in closed form. For solutions that are bounded at the origin and which vanish at infinity, the inverse Laplace transform then furnishes (4.6). Provided

$$\int_0^\infty d\rho\, \rho^2\, \hat{\zeta}^{(0)}(\rho) < \infty, \tag{4.8}$$

the exact solution is valid for arbitrary swirl profiles whose angular velocity is finite at the origin and whose large r behavior is no worse than a constant. This covers a wide variety of basic state velocity profiles of geophysical interest.

Smith and Rosenbluth developed this solution within a plasma physics context. The solution technique has been rediscovered by Reznik and Dewar (1994) in an analytical study of vortex motion on a beta plane. In both investigations, however, emphasis was directed at understanding its long time behavior and a detailed analysis of its transient dynamics was not considered. In the next section, the transient dynamics of the exact solution will be compared against the AB model.

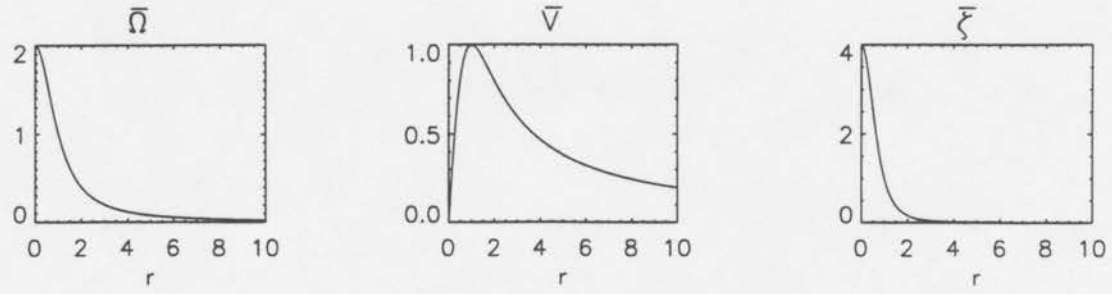

Figure 4.5: The non–dimensional basic state vortex used in the exact solution: $\bar{\Omega} = 2/(1+r^2)$, $\bar{v} = r\bar{\Omega}$, $\bar{\eta} = \bar{\Omega} + d\bar{v}/dr$. The model domain is of length 40, but only the inner 10 units are shown. Although this swirl profile falls off significantly faster than the benchmark vortex of the AB model, it is nevertheless stable to exponential disturbances.

4.6 Exact Solution Results: A Side–by–Side Comparison

From the form of the exact solution it is difficult to identify the nature of the transient solution. It may nevertheless be revealed by considering the evolution of wavenumber one asymmetries on the nondimensional basic-state swirl profile

$$\bar{v}(r) = \frac{2r}{1+r^2}. \tag{4.9}$$

The corresponding nondimensional angular velocity profile is

$$\bar{\Omega}(r) = \frac{2}{1+r^2}, \tag{4.10}$$

and characteristic length and velocity scales correspond to the radius of maximum winds, and the maximum tangential velocity, respectively, see figure 4.5. The model domain is of length 40 which corresponds to the domain of the AB benchmark vortex but only the inner 10 units are shown. Since the mean vorticity is a monotonic function of radius, the vortex satisfies Rayleigh's sufficient condition for exponential stability. Despite the fact that this vortex has an infinite integrated kinetic energy and angular momentum, the results shown below are not sensitively dependent on these properties and have been verified for other swirl profiles with finite energy and angular momentum.

Shown in figure 4.6 is the evolution of an initial wavenumber one disturbance ($\hat{\zeta}^0 = \exp[-(r-3)^2]$). This initial condition corresponds to the initial condition used in the AB model. The left column displays the Fourier vorticity–amplitude as a function of r,

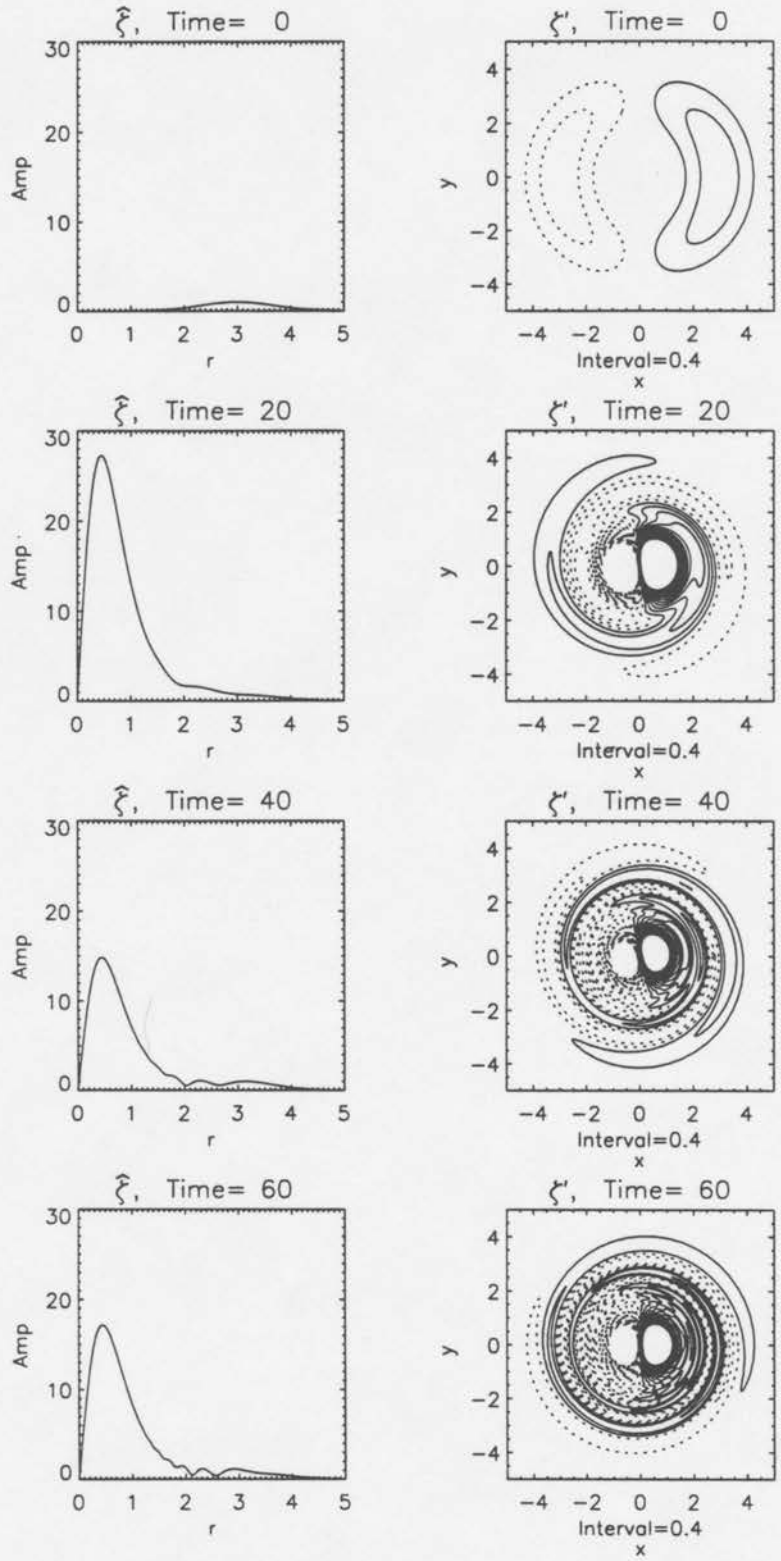

Figure 4.6: Time series showing the radial plots of $|\hat{\zeta}|$ (left panels) and horizontal plots of ζ' (right panels) for the Smith and Rosenbluth (1990) exact solution. The initial asymmetry is positioned at $r = 3$. For the sake of clarity values of $|\zeta'| > 3.8$ have not been contoured. Times correspond to 0.0, 3.2, 6.4, and 9.6 circulation times and the horizontal distance shown is five RMW units.

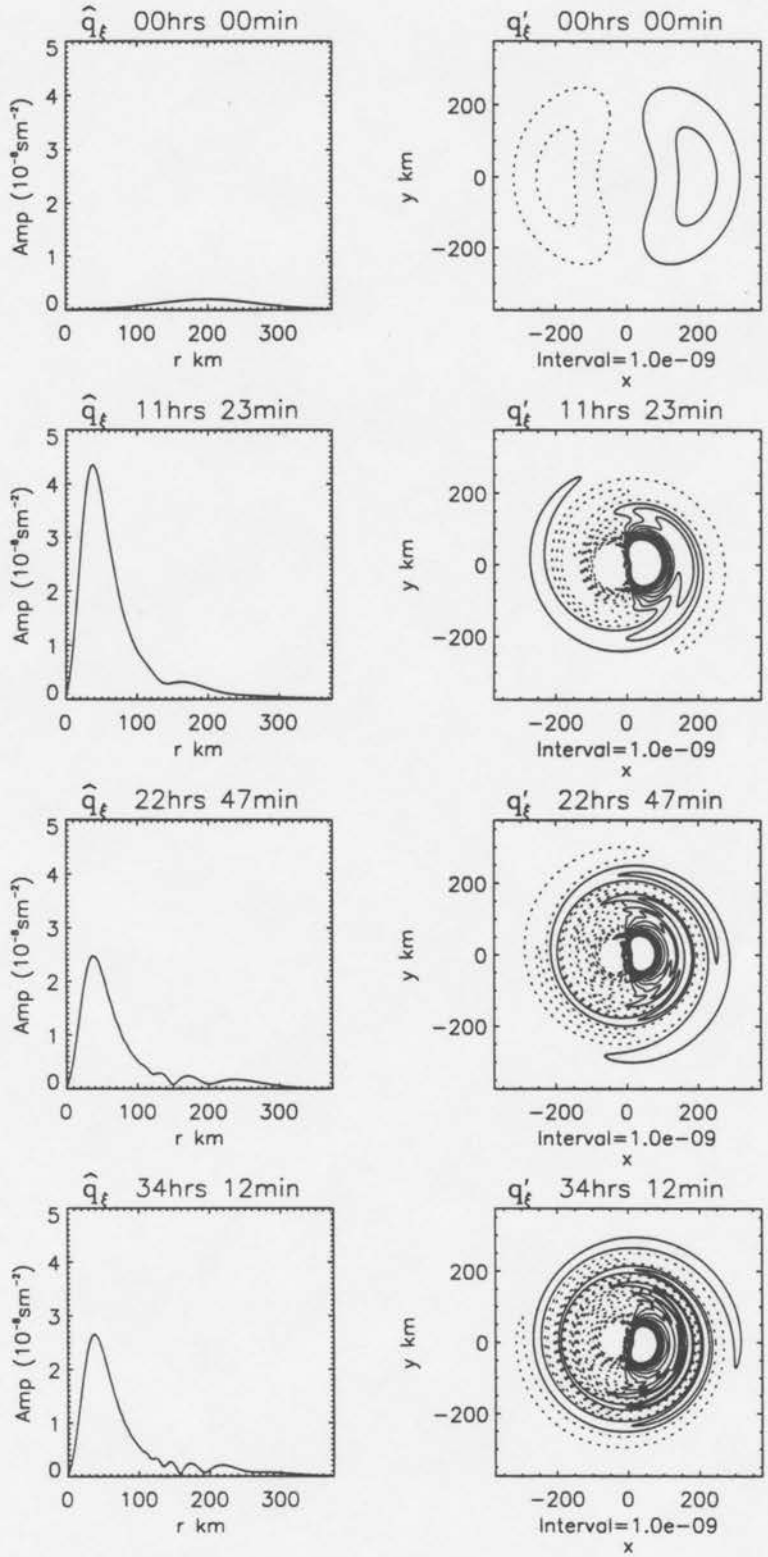

Figure 4.7: Time series showing the radial plots of $|\hat{q}_\xi|$ (left panels) and horizontal plots of q'_ξ (right panels) for the AB model. The initial asymmetry is positioned at $r = 200\ km$ (approximately three RMW units). For the sake of clarity values of $|q'_\xi| > 1.05 \times 10^{-8} sm^{-2}$ have not been contoured. Times correspond to 0.0, 3.2, 6.4, and 9.6 circulation times and the horizontal distance shown is five RMW units.

while the right column displays map plots of the asymmetric vorticity field. Negative values are enclosed in dashed lines. Contour values below and above $(-3.8/3.8)$ have been omitted for the sake of clarity. Shown in figure 4.7 is the evolution of an initial wavenumber one disturbance in the AB model. The left column displays the Fourier PV–amplitude as a function of r, while the right column displays map plots of the asymmetric PV field. Negative values are enclosed in dashed lines. Contour values below and above $(-1.05 \times 10^{-8}/1.05 \times 10^{-8}) sm^{-2}$ have been omitted for the sake of clarity. In both figures the times correspond to 0.0, 3.2, 6.4, and 9.6 circulation times and the horizontal distance shown is five RMW units. Both solutions display expected features consistent with theory and also show good qualitative agreement in the fine structure.

At a radius of $r = 0.4$ in the nondivergent model and $r = 40\ km$ in the AB model, we see the first of the expected features: the rapid emergence of the pseudo-mode. Taking the Laplacian of (4.3) reveals the vorticity field associated with the pseudo mode is maximum where $d\bar{\zeta}/dr$ is maximum, $r = 0.43$. The analogue of vorticity in the shallow water model is the potential vorticity $\hat{q}_\xi$ which displays a maximum at $r = 40\ km$ corresponding to where $d\bar{q}/dr$ is maximum. The pseudo mode is not the only interesting feature, however, found in the inner core. Superimposed on the pseudo mode is a transient algebraic growth and decay cycle. The larger growth growth observed in the nondivergent model can be traced to the differing influence scales in the divergent and nondivergent models. The nondivergent model permits a stronger radial flow across the mean vorticity gradient and results in larger algebraic growth. The trailing arms found in the nondivergent model lag behind those of the AB model because the nondivergent swirl profile decays faster than the AB swirl profile.

The exact solution at $t = 60$ shows the pseudo mode oriented due east. This compares to an orientation slightly south of east in the AB model at the corresponding time of $t = 34\ hrs\ 12\ min$. At much longer times, the pseudo mode in the exact solution slowly rotates at a dimensional angular velocity of $9 \times 10^{-7} s^{-1}$, as compared to $-1.3 \times 10^{-6} s^{-1}$ in the AB model. This is the boundary influence discussed in section 4.3. The rotation rate in the nondivergent model is proportional to b^{-2} where b is the position of the outer

boundary. Since the domains of the two models scale identically, the weak rotation of the pseudo mode in the shallow water model may also be dependent on the variable deformation radius.

Upon closer investigation, one also observes outward propagating waves between the inner-core and outer-core asymmetries. These waves are observed for $1.25 < r < 2.5$ in the exact solution and $120\ km < r < 230\ km$ in the AB model. The wave crests emerge at the edge of the pseudo-mode and travel outwards to a radius where their outward propagation ceases. The radial plots are especially useful for seeing this effect. The physics of these waves are elucidated in chapter 5. For now they will be used as another measure of model agreement. To further examine the outward wave propagation, radius-time plots were made of both models that track the radial location of wave crests in the Fourier vorticity and PV amplitude. Wave crests are identified by zeros in $d^3|\hat{\zeta}|/dr^3$ or $d^3|\hat{q}_\xi|/dr^3$. This analysis method purposely filters out individual phase features. The filter method may be illustrated by considering a Hankel function representation of an outgoing cylindrical wave of some field, $g(r)$, with given phase speed. The absolute value of the Hankel-function wave is time invariant and has no zeros in $d^3|g(r)|/dr^3$. This method is therefore naturally suited for determining radial group velocity.

Upon comparing the exact solution (figure 4.8 bottom panel) with that of the AB model for wavenumber one (figure 4.8 top panel), we see the detailed structure of the outward propagating waves is extraordinarily similar. The similarity persists despite the fundamental differences between the divergent and nondivergent models.[1]

Even fine details such as the "cusp" shape at $t = 9$ in the exact solution appear at $t = 5\ hrs$ in the AB simulation (1.4 circulation times in both models). In the exact solution the dimensional group velocity calculation for the first wavecrest at $(r, t) = (1.33,\ 15)$ is $1.3\ ms^{-1}$. A similar calculation for the first wavecrest at $(r, t) = (84\ km, 6\ hrs)$ in the AB simulation also yields $1.3\ ms^{-1}$. As another check of model consistency we note that the

---

[1]The wavecrest algorithm was unable to continuously track the leading asymmetry for the AB model. Detailed analysis of the radial plots, however, confirm that the leading asymmetry moved smoothly outwards on a radial trajectory suggested by the broken plot.

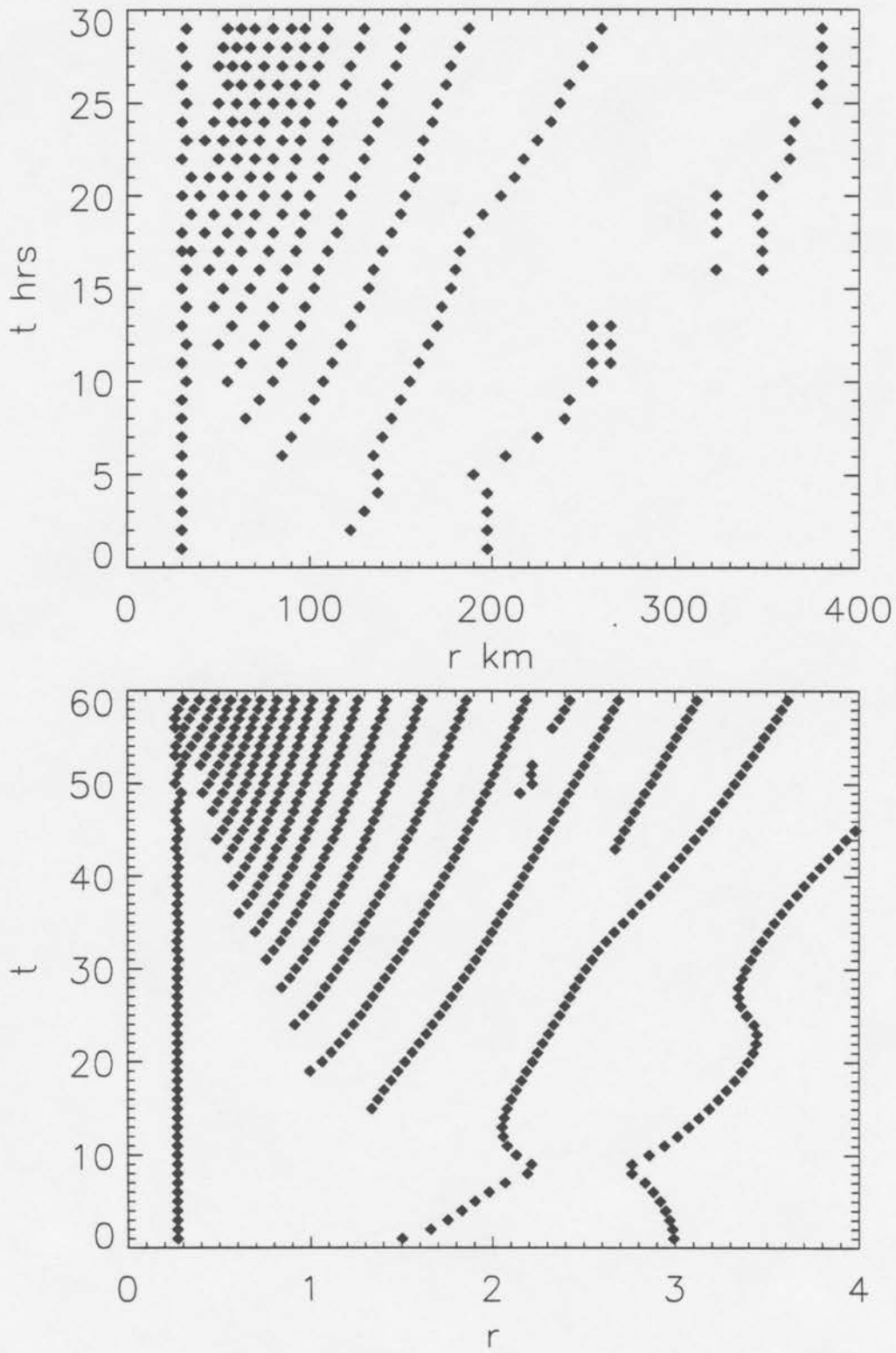

Figure 4.8: Radius-time plots showing migrating wavenumber one wavecrests in the AB model (top panel) and the Smith and Rosenbluth (1990) exact solution (bottom panel). The maximum time on each plot represents approximately 9 circulation times. The horizontal domain is five RMW units for the AB model which compares to four RMW units in the exact solution.

exact solution exhibits dispersion at $(r,t) = (2.5, 38)$, while the AB simulation exhibits dispersion at $(r,t) = (180\ km, 21\ hrs)$. Non-dimensionally, the latter corresponds to $(r,t) = (2.4, 37)$. The stationary feature is the pseudo mode in both models.

4.7 Summary

In this chapter the AB shallow water model has been further validated through a detailed analysis of wavenumber one evolution. Among the physical processes better understood is the manner by which wavenumber one moves the vortex. The analytical solution to the nondivergent model of GSM revealed that wavenumber one asymmetries project onto the pseudo mode through an interaction term. Reynolds stress plots of the AB model then give a physical interpretation to the interaction term. The steady pseudo mode emerges at long times and identifies the final position of the vortex.

Detailed comparison of the AB model with an exact solution of the linearized non-divergent model demonstrated remarkable agreement. Items of agreement included the emergence of the pseudo mode and radially propagating vorticity waves. Even specific measurements such as wave speed and location agreed within a few percent.

Understanding the transient dynamics and the pseudo mode reveals that it may be possible to diagnose storm motion in the linear model from the current geopotential field. The method may entail extracting that portion of the geopotential tendency which has the same radial structure as $\bar{v}(r)$. Extracting this portion of the signal may prove straightforeward because of the dominance of the contribution involving storm motion. Knowing the contribution of the tendency of wavenumber one which projects onto storm motion and the structure of $\bar{\Phi}(r)$ allows the new center to be determined. The vortex motion can then be incorporated into a moving grid which will remain at the center of the vortex every forecast step.

Chapter 5

VORTEX ROSSBY WAVES

5.1 Introduction

Chapter 3 showed that fine–scale PV waves are natural byproducts of the symmetrization process in regions possessing a nonzero basic state PV gradient. High temporal resolution reveals that such fine structures are radially propagating waves accompanying the algebraic decay cycle described in section 3.4. Their robustness was further demonstrated by an exact solution of the nondivergent model for wavenumber one. Finally and most importantly, the symmetrization process produced structures which exhibited qualitative similarities to hurricane spiral bands.

Two main theories have been proposed to explain the physics of outward–propagating hurricane bands. The first theory describes these features as outward–propagating gravity-inertia waves (Abdullah 1966; Kurihara 1976), while the second describes them as sheared PV disturbances (GS). Given the fine-scale structure and outward propagation of the inner bands, one might naturally suspect them to be gravity-inertia waves. However, since both inner and outer bands are often observed to propagate slower than the local mean flow (Senn and Hiser 1959; Powell 1990; May 1995), their basic dynamics may instead lie rooted in the "slow-manifold" associated with the advective component of the flow. Spiral bands were qualitatively described as vortex Rossby waves by MacDonald (1968). Unlike planetary Rossby waves, which owe their existence to the meridional gradient of planetary PV, vortex Rossby waves were postulated to exist on the radial gradient of storm PV. Following this theme, GS presented perhaps the most penetrating investigation of hurricane spiral bands to date. In the context of PV dynamics, GS demonstrated that a shallow water primitive equation model evolves banded features with minimal projection

on the gravitational linear-wave manifold. For the elliptical vortex case of GS, the banded features studied probably correspond to the leading wave packet observed in the radius–time plots of this chapter and chapter 4. However, the link between the symmetrization process, algebraic growth, and fine–scale outward–propagating PV waves was not the subject of their study.

In this chapter we focus on the problem of outward–propagating bands in vortex flows. Their structure will be examined within the context of PV dynamics. The bands are described as outward–propagating vortex Rossby waves on an f-plane that are ultimately sheared by the differential rotation of the vortex.

5.2 Wavenumber One

As demonstrated in section 4.6, the exact nondivergent and AB models behave remarkably alike for stable vortices. Further examination reveals three other noteworthy characteristics in figure 4.8. The first is the tendency of individual wave crests to slow as they move outwards. Secondly, the radial wavenumber increases and the corresponding radial group velocity decreases at long times. Thirdly, we observe dispersion in two instances where wave crests emerge at $(r,t) = (2.16, 49)$ and $(r,t) = (2.68, 43)$ which correspond to dimensional units of $(160\ km, 28\ hrs)$ and $(200\ km, 24\ hrs)$ respectively. The results suggest an important wave dynamic operating in vortex flows whereby disturbances may extract energy from the vortex at one radial band and deposit it at another radial band. Whether or not such processes are operative for higher wavenumbers is the subject of the next section.

5.3 Higher Wavenumbers

Higher wavenumbers exhibit symmetrization and radial wave propagation without the complication of the pseudo-mode. As representative of higher wavenumbers, wavenumbers two and three are examined in detail below.

As an illustration, consider idealized asymmetries forced by convection in the eyewall of a hurricane:

$$\hat{q}_\xi^{(0)} = 2 \times 10^{-8} sm^{-2} \exp\left[-\left(\frac{(r - 75\ km)}{50\ km}\right)^2\right]. \tag{5.1}$$

The evolution summarized in figure 5.1 shows perhaps the simplest case of outward–propagating shear waves.

Initially, the leading wavenumber two wave packet moves from $r = 75\ km$ to $r = 120\ km$ where outward propagation ceases (figure 5.1 top panel). Almost immediately the initial disturbance has induced an inner-core asymmetry near the maximum of the basic state PV gradient. This asymmetry then emits wave packets which propagate outward to 75 km where again outward propagation ceases. The radius at which outward propagation ceases will henceforth be referred to as the stagnation radius, cf. Tung (1983). As will be shown, the stagnation radius is not unique and depends on the initial wave location and radial structure. The fact that the inner wave crests find their stagnation radius at 75 km is merely coincidental and has nothing to do with the RMW nor the location of the initial asymmetry. An additional feature to note is the stationary wave crest at 25 km ends when the wave activity at other radial locations end. This marks the completion of symmetrization when the asymmetry can no longer force an inner–core response.

The bottom panel of figure 5.1 shows that the symmetrization of wavenumber three is accompanied by much less radial wave activity. Similarly to wavenumber two, the initial wave crest reaches its stagnation radius at 110 km. Also, the forced inner–core response ends approximately when the wave activity ends elsewhere.

Figure 5.2 shows radius time plots of wavenumbers two and three initially at $r = 200\ km$. For wavenumber two, the stagnation radius of the initial disturbance at first appears as though it would be 240 km. But the wave crest nearing 200 km at $t = 15\ hrs$ interferes with the initial packet and moves the stagnation radius out to 260 km. Although a similar interference effect may have occurred for wavenumber three at $t = 13\ hrs$ it evidently didn't change the stagnation radius of 230 km. Radial plots (not shown) indicate the stagnation radius of the inner wavenumber two asymmetry is 200 km and that of the wavenumber three case is 150 km. Generally, as the center of the initial condition is placed at greater radii, two qualitative differences are noted. First, the inner-core asymmetries are observed to propagate beyond the radius of maximum wind; and secondly, many more wave crests are observed. Since distant asymmetries symmetrize more slowly, they

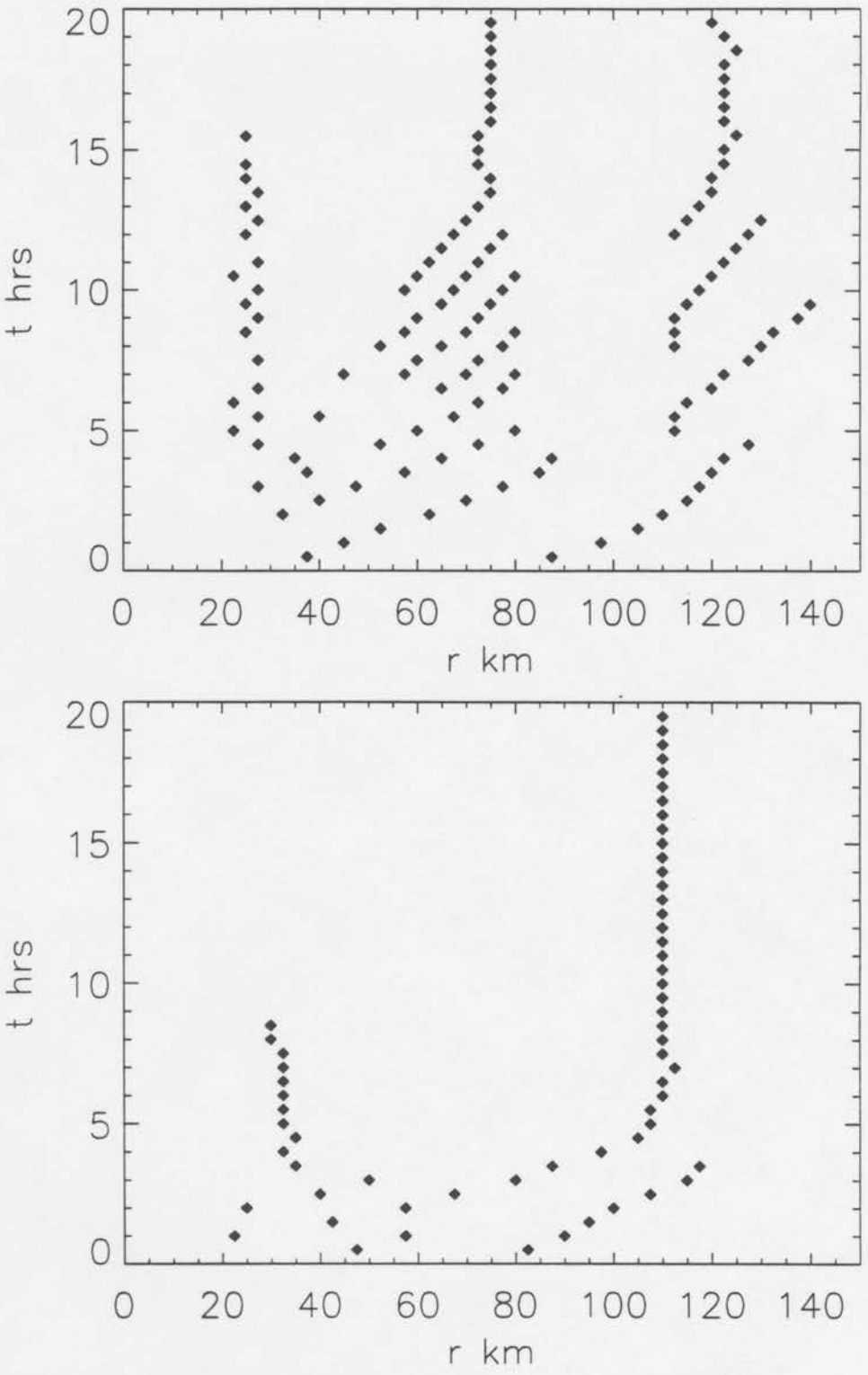

Figure 5.1: Radius-time plots showing migrating wave crests in the AB model for wavenumbers two (top panel) and three (bottom panel). The maximum time represents approximately 9 circulation times. The initial asymmetry was located at 75 km and had an e–folding distance of 50 km for both wavenumbers. For wavenumber two the stagnation radius of the outer asymmetry is approximately 120 km and that of the forced inner response is coincidentally 75 km. For wavenumber three the stagnation radius of the outer asymmetry is 110 km. In both cases, the stationary response in the inner–core ends when the outer wave crest reaches its stagnation radius.

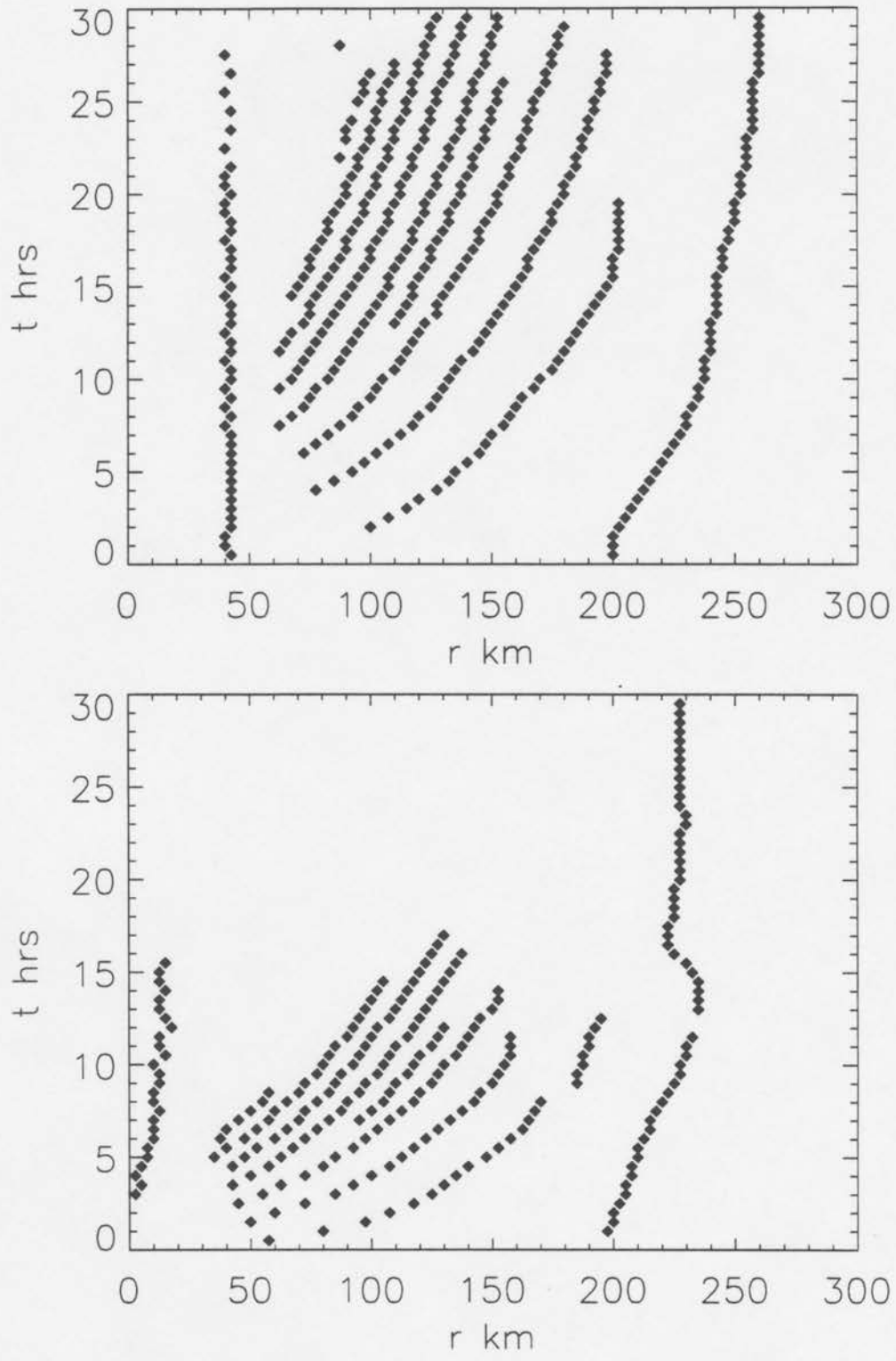

Figure 5.2: Radius-time plots showing migrating wave crests in the AB model for wavenumbers two (top panel) and three (bottom panel). The maximum time represents approximately 9 circulation times. The initial asymmetry was located at 200 km and had an e–folding distance of 100 km for both wavenumbers. For wavenumber two the stagnation radius of the outer asymmetry is 260 km and that of the forced inner response is 200 km. For wavenumber three the stagnation radius of the outer asymmetry is 230 km and that of the forced inner response is 150 km. In both cases, the stationary response in the inner–core ends when the outer wave crest reaches its stagnation radius.

appear as quasi-steady forcing to the inner core. The result is a series of wave-shedding events terminating when the outer disturbance has decayed sufficiently to force a negligible inner-core response. This example may have important meteorological applications since it raises the possibility that stationary environmental forcings may continuously excite radially propagating shear waves in the near-core region of a hurricane vortex.

Comparing the results for wavenumbers two and three shows radial wave-propagation effects diminish with increasing azimuthal wavenumber. At very high wavenumbers ($n >> 2$) radial propagation is virtually non-existent and outer-core asymmetries induce almost no inner-core response. The latter property is easily traced to the wavenumber-dependent influence scale that relates PV to geopotential. The former property will be explained in section 5.4. Taken together, these experiments indicate that for a stable vortex, asymmetric dynamics for high wavenumbers is qualitatively similar to the bounded Rankine vortex (SM).

5.4 WKB Analysis

The behavior of the exact solution and the AB results show outward–propagating PV waves often possess radial length scales (l) that are small compared to the characteristic radial scale (L) of the vortex. Under such conditions it is justifiable to seek approximate solutions near $r = R$ in the form

$$\phi'(r,\lambda,t) \sim A(t)\exp\Big[i\Big(n\lambda + k(t)(r-R) - \Lambda(t)\Big)\Big], \tag{5.2}$$

where $A(t)$ is a time-dependent amplitude, $k(t)$ a time-dependent radial wavenumber, and $\Lambda(t)$ a time-dependent phase. Since (5.2) is expected to describe sheared disturbances we may without loss of generality assume that A is real-valued. Provided $l << L$, basic-state variables can be assumed slowly varying and may be expanded in series:

$$\bar{q}(r) = \bar{q}_\circ + \bar{q}'_\circ\,\delta r + ...$$

$$\bar{\xi}(r) = \bar{\xi}_\circ + \bar{\xi}'_\circ\,\delta r + ...$$

$$\bar{\gamma}^2(r) = \bar{\gamma}^2_\circ + \bar{\gamma}^{2\prime}_\circ\,\delta r + ...$$

$$\bar{\Omega}(r) = \bar{\Omega}_\circ + \bar{\Omega}'_\circ\,\delta r + ...$$

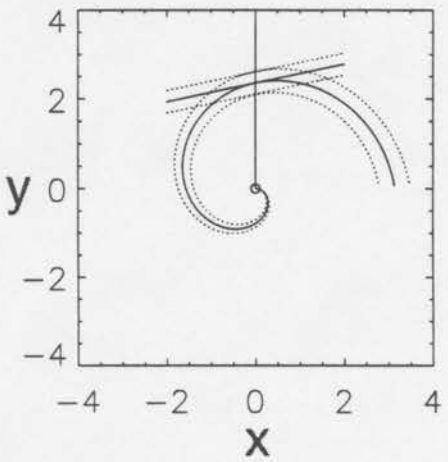

Figure 5.3: Schematic of a local plane-wave approximation to a trailing spiral in the WKB formulation. The solid line represents the wave crest and the dashed lines represent neighboring wave troughs. The x and y scales are in terms of RMW units.

$$\frac{d\bar{q}}{dr}(r) = \bar{q}_o' + \bar{q}_o''\,\delta r + \ldots$$
$$\frac{1}{r} = \frac{1}{R}\left(1 - \frac{\delta r}{R} + \ldots\right), \tag{5.3}$$

where $\delta r = r - R$, prime denotes differentiation with respect to radius, and the zero subscript denotes evaluation at $r = R$. On substituting (5.2) and (5.3) into the forecast equation (2.30), neglecting terms of $O((kR)^{-1},\ \delta r/R)$, assuming $\frac{r}{\bar{\gamma}^2}\frac{d\bar{\gamma}^2}{dr}$ is O(1), and equating real and imaginary parts to zero gives, respectively

$$\dot{A}\left(k^2 + \bar{\gamma}_o^2 + \frac{n^2}{R^2}\right) + 2k\dot{k}A = 0, \tag{5.4}$$

$$\left(k^2 + \bar{\gamma}_o^2 + \frac{n^2}{R^2}\right)\left(\dot{\Lambda} - n\bar{\Omega}_o\right) - \frac{n\bar{\xi}_o}{R\bar{q}_o}\,\bar{q}_o' - \left(k^2 + \bar{\gamma}_o^2 + \frac{n^2}{R^2}\right)\left(\dot{k} + n\bar{\Omega}_o'\right)\delta r = 0, \tag{5.5}$$

where dot denotes differentiation with respect to time. In the derivation of (5.5) the term $n\bar{q}_o''\bar{\xi}_o\,\delta r/(\bar{q}_o R)$ has been neglected. When this term is compared with $(k^2 + \bar{\gamma}_o^2 + n^2/R^2)\ n\bar{\Omega}_o'\,\delta r$, it is found to scale as $O\{(kR)^{-1} \times (kL)^{-1}\}$. Thus provided kL is not small, the term in question is of the same order as terms already neglected.

Equations (5.4) and (5.5) are integrated as follows. Since (5.5) is valid for small, but otherwise arbitrary δr, setting $\delta r = 0$ furnishes the instantaneous wave frequency

$$\dot{\Lambda}(t) = n\Omega_o + \frac{n\bar{\xi}_o}{R\bar{q}_o}\frac{\bar{q}_o'}{(k^2 + \bar{\gamma}_o^2 + \frac{n^2}{R^2})}. \tag{5.6}$$

Because $k^2 + \bar{\gamma}_o^2 + n^2/R^2$ is never zero this in turn implies

$$\dot{k} = -n\bar{\Omega}_o'$$

whose integration yields

$$k(t) = k_o - nt\,\bar{\Omega}_o', \tag{5.7}$$

where k_o is an initial radial wavenumber. Equations (5.4) and (5.5) then furnish

$$A(t) = \frac{\left(k_o^2 + \bar{\gamma}_o^2 + \frac{n^2}{R^2}\right)A_o}{(k_o - nt\bar{\Omega}_o')^2 + \bar{\gamma}_o^2 + \frac{n^2}{R^2}}, \tag{5.8}$$

where A_o is the initial wave-amplitude. Expressions (5.7) and (5.8) represent the cylindrical analogue of sheared disturbances in rectilinear simple-shear flow and the solutions

are well known. The derivation of (5.6) in the context of axisymmetrizing disturbances, however, is believed new.

Equation (5.6) can be shown to represent the local dispersion relation

$$\omega = n\Omega_\circ + \frac{n\bar{\xi}_\circ}{R\bar{q}_\circ}\frac{\bar{q}'_\circ}{(k^2+\bar{\gamma}_\circ^2+\frac{n^2}{R^2})} \tag{5.9}$$

for a spectrally localized wave packet whose initial central wavenumbers are $k_\circ$ and n, respectively (cf. Tung 1983; Yamagata 1976). This dispersion relation is analogous to the dispersion relation for nondivergent Rossby waves on a beta-plane in a uniform zonal wind. The meridional derivative of planetary PV is replaced by the radial derivative of basic-state storm PV, while the Doppler-shifted frequency is replaced by the azimuthal wavenumber times the basic-state angular velocity. For a cyclonic monopole whose basic state possesses an everywhere negative radial PV gradient, the dispersion relation predicts that individual waves retrogress relative to the local angular velocity. Unlike Rossby waves on a beta plane, however, the radial wavenumber is ever-changing due to the symmetrizing effect of the vortex. As we will see this has fundamental consequences on the kinematics and dynamics of vortex wave-packets.

Radial and azimuthal phase velocities, defined by $C_{pr} = \omega/k$ and $C_{p\lambda} = \omega R/n$ are given by:

$$C_{pr} = \frac{n}{k}\bar{\Omega}_\circ + \frac{n\bar{\xi}_\circ}{Rk\bar{q}_\circ}\frac{\bar{q}'_\circ}{(k^2+\bar{\gamma}_\circ^2+\frac{n^2}{R^2})}, \tag{5.10}$$

$$C_{p\lambda} = R\bar{\Omega}_\circ + \frac{\bar{\xi}_\circ}{\bar{q}_\circ}\frac{\bar{q}'_\circ}{(k^2+\bar{\gamma}_\circ^2+\frac{n^2}{R^2})}. \tag{5.11}$$

The speed and direction of energy propagation, however, is controlled by the group velocity whose radial and azimuthal components, defined by $C_{gr} = \partial\omega/\partial k$ and $C_{g\lambda} = \partial\omega/\partial(n/R)$ are given by:

$$C_{gr} = \frac{-2kn\bar{\xi}_\circ\bar{q}'_\circ}{R\bar{q}_\circ(k^2+\bar{\gamma}_\circ^2+\frac{n^2}{R^2})^2}, \tag{5.12}$$

$$C_{g\lambda} = R\bar{\Omega}_\circ + \frac{\bar{\xi}_\circ}{\bar{q}_\circ}\frac{\bar{q}'_\circ}{(k^2+\bar{\gamma}_\circ^2+\frac{n^2}{R^2})^2}\left[k_\circ^2+\bar{\gamma}_\circ^2-\frac{n^2}{R^2}(1+t^2R^2\bar{\Omega}_\circ'^2)\right]. \tag{5.13}$$

In (5.9 – 5.13), k is given by (5.7).

To fix ideas consider the simple case of a cyclonic monopole with a non-positive $\bar{q}'_\circ$. A hypothetical spiral that spirals cyclonically inwards is sketched in figure 5.3. Portions of this spiral can be described by

$$kr + n\lambda = \text{constant},$$

and n may be assumed positive without loss of generality. Since a trailing spiral is associated with positive k, its corresponding radial group velocity is positive. *Hence, symmetrizing disturbances on vortex monopoles always have an outward directed group velocity.* This is quite unlike the behavior of sheared disturbances in a uniform PV environment that have zero group velocity in the cross-shear direction. As the packet propagates outward it is continually slowed by the shearing effect that increases its radial wavenumber. Since for large k the radial group velocity goes as $O(k^{-3})$ the shearing effect eventually dominates and radial propagation ceases. This describes the stagnation radii of section 5.3. The radial trajectory of an isolated wave packet may be obtained from a time integral of the radial group velocity (cf. Tung 1983):

$$r(t) = R + \frac{\bar{\xi}_\circ}{\bar{q}_\circ}\frac{\bar{q}'_\circ}{R\bar{\Omega}_\circ}\left\{\frac{1}{(k_\circ^2 + \bar{\gamma}_\circ^2 + \frac{n^2}{R^2})} - \frac{1}{(k_\circ - nt\bar{\Omega}'_\circ)^2 + \bar{\gamma}_\circ^2 + \frac{n^2}{R^2}}\right\}, \tag{5.14}$$

where $r(t)$ denotes the instantaneous radial position of the wave packet. The stagnation radius, r_s, results by letting $t \to \infty$:

$$r_s = R + \frac{\bar{\xi}_\circ}{\bar{q}_\circ}\frac{\bar{q}'_\circ}{R\bar{\Omega}'_\circ}\frac{1}{(k_\circ^2 + \bar{\gamma}_\circ^2 + \frac{n^2}{R^2})}. \tag{5.15}$$

Similar reasoning suggests that leading spirals (i.e. disturbances possessing an upshear tilt; $k_o < 0$) have an inward directed group velocity. In this case environmental asymmetries can excite inward–propagating waves until their radial wavenumber changes sign, after which they would begin their outward propagation. Though one might naively suspect that highly tilted upshear and downshear initial conditions are equally likely, physical consideration of hurricane vortices strongly favors trailing spirals. Further discussion of this point is reserved for section 5.5.1.

Inferences about azimuthal kinematics can also be deduced. For $k_oR >> 1$, (5.13) shows that $C_{g\lambda} - R\bar{\Omega}_\circ$ is initially negative. As the packet propagates outward, however,

$C_{g\lambda} - R\bar{\Omega}_o$ quickly becomes positive and ultimately asymptotes to zero at long times. The latter effect resembles the behavior of the zonal group velocity for simple Rossby waves on a beta-plane. As the shearing effect predominates, the total wavenumber becomes large. Instead of the packet always retrogressing, it temporally moves faster than the mean wind until it is sheared by the differential rotation of the vortex.

Although inferences drawn above may be of a general nature, the case of an unstable vortex requires understanding how instability growth and saturation interact with the wave processes examined here. This interesting topic remains for future work.

5.4.1 WKB Validation

To test the usefulness of the WKB approximation developed above, time integrations of WKB group velocity and AB radius-time plots are now compared. Since the radial length-scale of the outer initial condition used in the AB integration has roughly the scale of the radius of maximum wind, $k_o = 1/RMW$ seems an appropriate choice. The inner asymmetry was narrower making $k_o = 1.5/RMW$ more appropriate. Because the WKB approximation assumes $kR >> 1$, $R = RMW$ is the inner most radius for which we might hope the approximation to be valid.

The WKB method is a local approximation that ignores distant influences. From figure 4.6 and the discussion of section 4.4 we observe that the pseudo mode is a quasi-steady phenomenon that influences the shape and evolution of radially propagating waves in the near-core region. Because of this limitation, we should only expect qualitative similarity between the WKB approximation and the observed radial propagation for wavenumber one. WKB results for wavenumber one (not shown) show a larger discrepancy with the AB and exact solution calculation than that noted below for higher wavenumbers. The foregoing limitations may be manifesting themselves in the representation for $k(t)$ since the observed group velocities lie between group velocities calculated for $k = k_o$ and $k = k_o - nt\bar{\Omega}'_o$. In addition, the results also show that wavenumber-one features travel a significant radial distance violating the local assumptions used to derive $k(t)$.

Figure 5.4 shows WKB radial group trajectories for wavenumbers two and three calculated by integrating the expression for C_{gr} (5.12) using the benchmark vortex basic

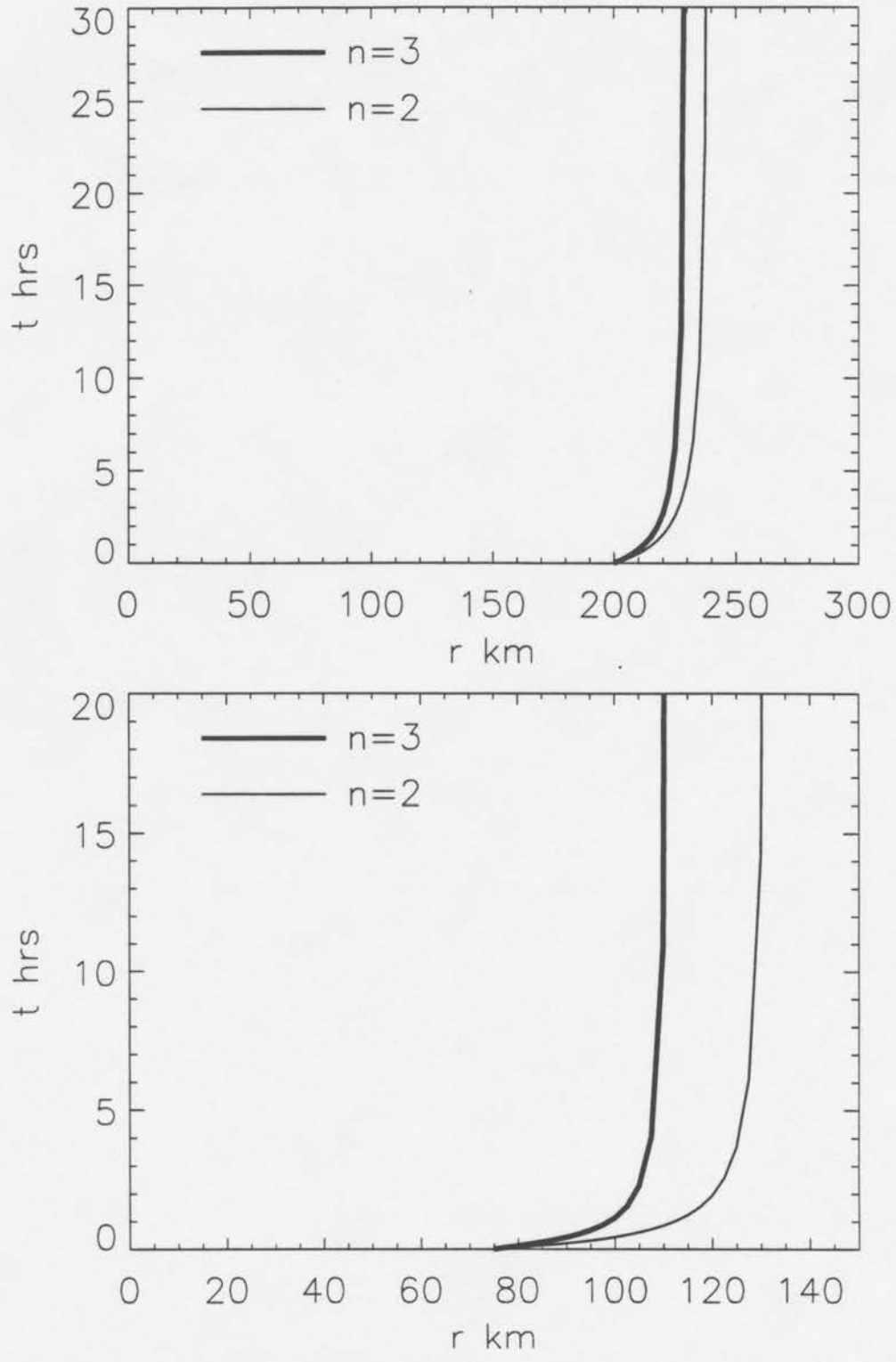

Figure 5.4: WKB radial wave–packet trajectories for wavenumbers two and three calculated by integrating the expression for C_{gr} using the AB benchmark vortex. The top panel shows results using $r_o = 200\ km$, $k_o = 1/RMW$, while the bottom panel uses $r_o = 75\ km$, $k_o = 1.5/RMW$.

state quantities. The top panel shows results using $r_o = 200\ km$ and $k_o = 1/RMW$ and the bottom using $r_o = 75\ km$ and $k_o = 1.5/RMW$. The top panel of figure 5.4 predicts the stagnation radii observed in figure 5.2 and the bottom predicts for figure 5.1. The WKB approximation duplicates the character of radial propagation observed in the AB model quite well. Especially noteworthy is the replication of the asymptotic ($t \rightarrow \infty$) behavior of radially propagating wave packets. For the initial condition at $r = 200\ km$, the AB model shows that wavenumbers two and three asymptote to $r = 260\ km$ and $r = 230\ km$, respectively while WKB theory asymptotes to $r = 240\ km$ and $r = 230\ km$ respectively. As was noted in section 5.3, the final stagnation radius of the leading wave packet was influenced by another wave packet thus violating the locality assumption. The first stagnation radius was 240 km which is the location prediction by the WKB radial group velocity. For the initial condition at $r = 75\ km$, the AB model shows that wavenumbers two and three asymptote to $r = 120\ km$ and $r = 110\ km$ respectively, while WKB theory asymptotes to $r = 130\ km$ and $r = 110\ km$ respectively. The WKB plots show faster movement from the initial R to the asymptotic r value. This discrepancy may be attributed to the tightly wound assumption of the WKB theory. This condition is not met for the initial disturbance which must evolve for some time before becoming tightly wrapped. Another factor that may contribute to the discrepancy is that the radial displacement is $O(1)$, pushing the local assumptions used to derive $k(t)$. For higher wavenumbers (not shown) radial wave propagation diminishes. The WKB predictions are consistent with this behavior by virtue of the n^{-3} dependence of C_{gr}.

The ability of the WKB method to forecast basic observed features of radial wave propagation gives us confidence in the asymptotic formulation. The functional dependence of both phase and group velocities on the basic-state PV gradient clearly indicates that such wave features are indeed vortex Rossby waves, confirming early speculations of MacDonald (1968).

5.5 Application to Hurricanes

5.5.1 Limitation of upshear tilt and algebraic growth

Initially, a migratory trough may be tilted upshear as it approaches the vortex. As with any synoptic scale pattern, however, the approaching trough is typically larger than the vortex. This implies that large upshear-tilt geometry will exist only locally, with the rest of the trough being nearly upright. In the analogous plane-wave model on the other hand, perturbations are easily configured to have large upshear tilt throughout the domain. This gives the plane-wave model the potential for much greater growth. To produce large algebraic growth (e.g., Farrell 1987), vortex perturbations must be tightly wound, anticyclonic spirals. This is unlikely in the face of cyclonically spiraling inflow and a large anticyclonic shear that tends to force cyclonic spirals.

The scale difference is one reason downshear tilt is forced, but another is the radially varying basic-state shear. A small portion of the trough imagined above will have a significant inward group velocity. The inward directed wave will then encounter ever-increasing shear, quickly changing the upshear configuration to downshear (cf. section 5.4). This results in a fast reversal to outward motion. The conclusion is similar to that of Tung (1983) who considered the dynamics of planetary Rossby wave packets in rectilinear simple-shear flow. Tung's formulation, however, did not consider latitudinal variation of the basic state shear. Consequently in the vortex case we expect much less inward motion.

Eyewall convection, on the other hand, may produce asymmetries with any orientation relative to the horizontal shear. But there is no reason to suspect that upshear tilt is preferred. In fact, recent radar analyses by Tuttle and Gall (1995) show the opposite to be true, with trailing spirals predominating in the near-core region. The foregoing discussion does not rule out transient algebraic growth nor minimize its importance. We merely point out a realistic limitation of algebraic growth and inward propagation within hurricane-scale vortices.

5.5.2 Radar Observations

Using a wavelet analysis technique on radar reflectivity fields, Tuttle and Gall (1995) studied the nature of small-scale spiral bands observed in two hurricanes. Several hours of continuous radar coverage for hurricanes Andrew (1992) and Hugo (1989) were provided them by the Hurricane Research Division of NOAA (figure 5.5). Their analysis revealed remarkably detailed near-core structures with curious characteristics. These characteristics and their potential relationship to the current work are noted below.

Outward propagation:

A general outward propagation was observed for enhanced radar reflectivity values in the near-core. The radius–time plot (figure 5.6) shows an outward velocity for these features of approximately $4ms^{-1}$. This is in good agreement with velocity estimates calculated from figure 5.2 for wavenumber two. For the first several wave packets emanating from the inner-core, the velocity is between 2.5 and $3.5ms^{-1}$. Also noted in figure 5.6 is a stationary wave feature at 95 km, about 3 times the radius of maximum winds. For the inner-core wavenumber two asymmetries of figure 5.2, the stagnation radius is also approximately 3 times the radius of maximum winds.

Wave length:

The wavelet-analysis wavelength used was 10 km, corresponding to the approximate scale of the reflectivity bands. This analysis tends to suppress scales smaller and larger than 10 km. Close examination of figures 5.6 and 5.7, show there are several regions of the storm where the radial wavelength of the inner bands may be on the order of 20 km, or at least different than 10 km. Figures 5.2 and 5.1 show that much of the near-core wave activity in the AB model exhibits a radial wavelength between 10 and 25 km.

Possible cause:

Tuttle and Gall (1995) speculate that the fine structure of the near-core region is consistent with boundary-layer roll theory (Fung 1978), but also admit further detailed kinematic information is needed for a complete confirmation. Perhaps a more plausible explanation is radially propagating vortex Rossby waves. The associated vertical velocity couplet propagating with the PV wave will alternately enhance and suppress convection in

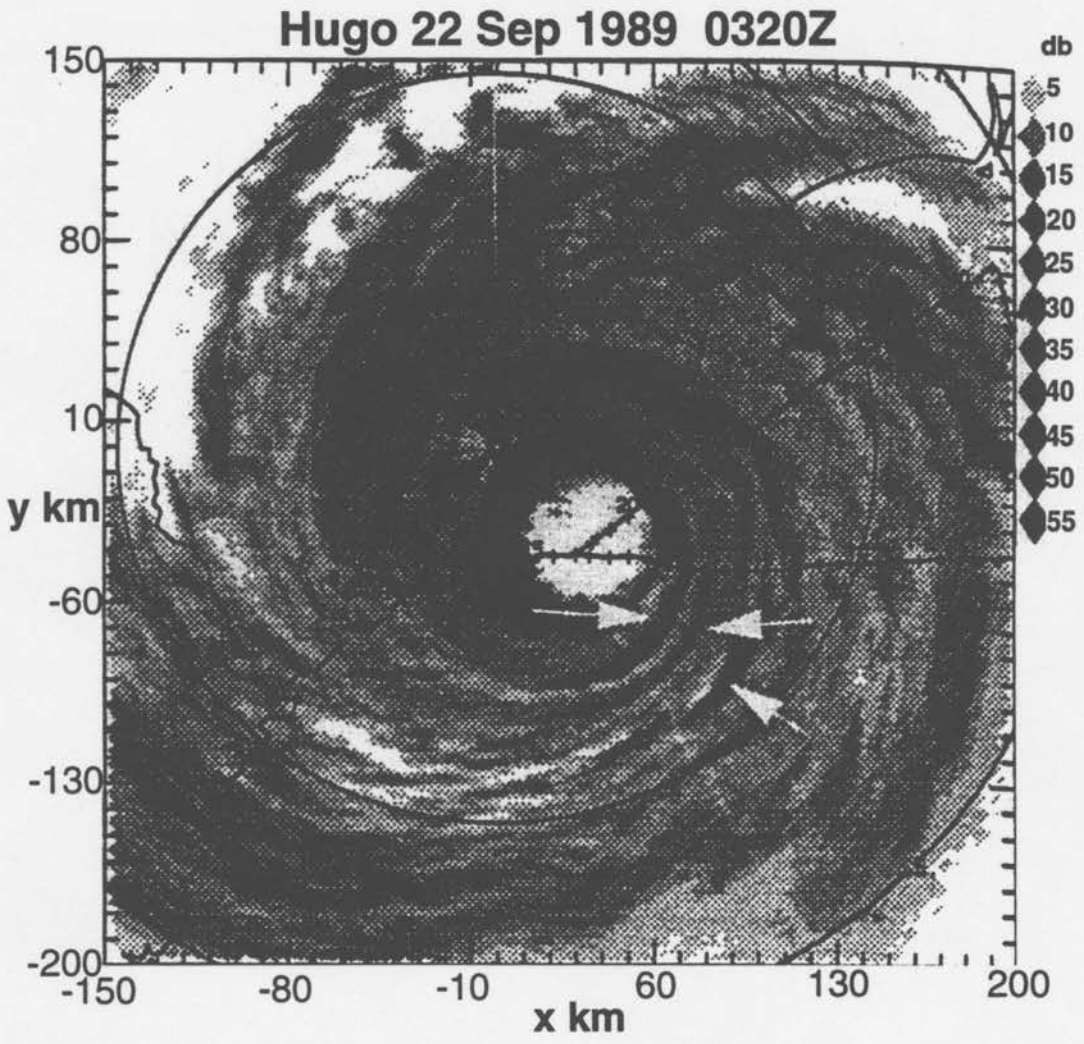

Figure 5.5: Tuttle and Gall's (1995, figure 1). WSR–57 radar reflectivity of Hurricane Hugo. Storm relative P3 track and geography are superposed. Arrows denote reflectivity bands. Reflectivity values start at 5 dBZ and increment by 5 dB.

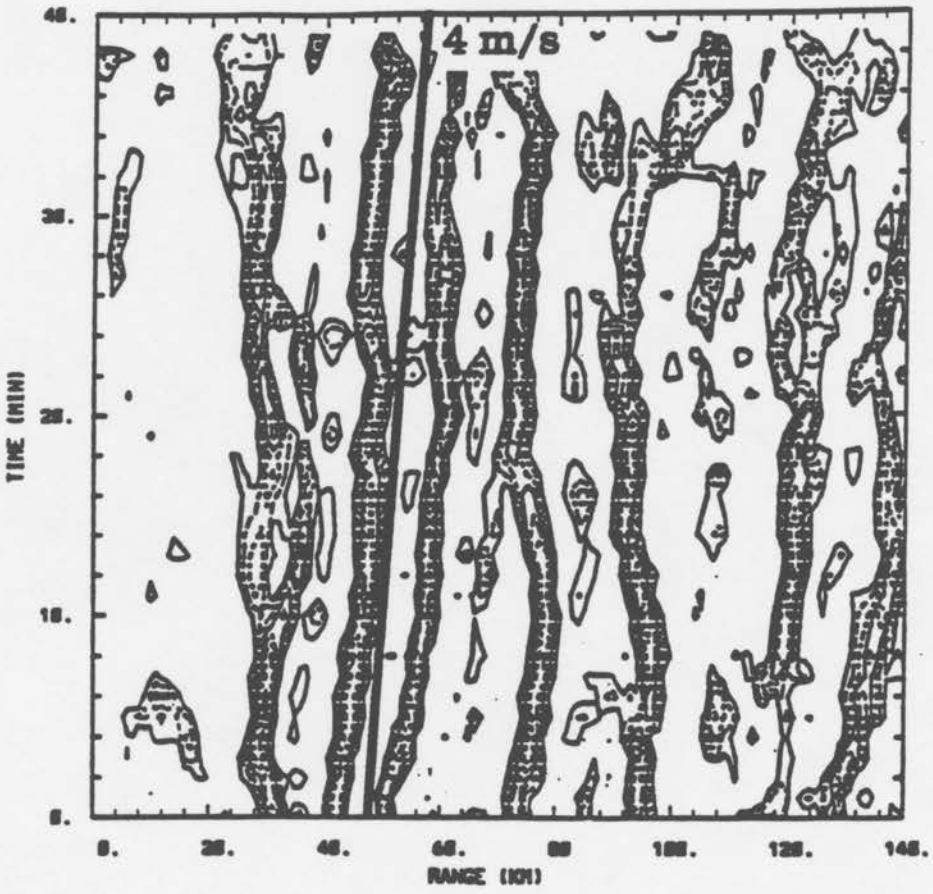

Figure 5.6: Tuttle and Gall's (1995, figure 6). Range–time correlation plot along segment shown in time sequence plots. Time is indicated along the vertical axis and is in minutes from 3:15Z. An outward propagation reference line of 4 ms^{-1} is shown.

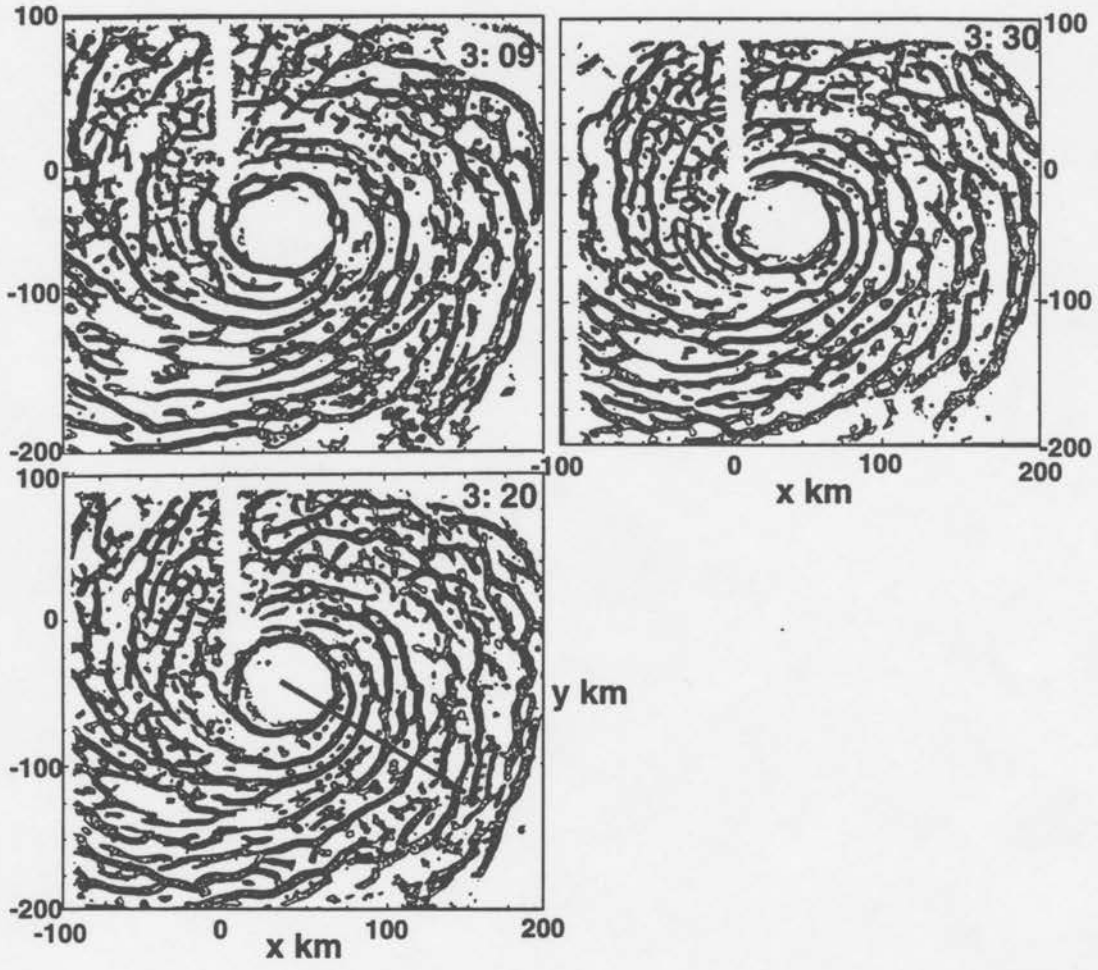

Figure 5.7: Tuttle and Gall's (1995, figure 5). Time sequence correlation values after applying wavelet analysis to Hugo reflectivity data. A spatial filter of 10 *km* was employed. Times are about 10 *min* apart. Contours start at 0.3 correlation coefficient and increment by 0.1. Line segment at 3:20Z shows location for the range–time correlation plot.

the moist environment of the near-core region. Map plots showing the symmetrization process in chapters 3 and 4 show the long trailing spiral structure of the outward–propagating waves is qualitatively similar to the map plots of figure 5.7. One can imagine in the case of spectrally broad continuous forcing, the clean results exhibited in the symmetrization map plots of chapters 3 and 4 will become noisy, more like that shown in figure 5.7 .

5.6 Summary

To better understand the potential importance of vortex Rossby waves in vortex evolution and structure changes, an inviscid wave mechanics was developed. Expressions for the group velocity were derived using WKB theory. Radial wave-packet trajectories were consistent with AB simulations in regions of the vortex where the WKB assumptions were valid. Their dispersive nature and their dependence on the vortex PV gradient justifies their designation as vortex Rossby waves.

The kinematics of individual wave packets show the existence of a stagnation radius which provides a site for wave mean-flow interaction. In the presence of convective forcing this process represents an asymmetric spin-up mechanism that could be operative in the formative stages of tropical cyclones. At later stages in the hurricane life cycle this process is consistent with the formation of secondary wind maxima.

In summary the wave mechanics developed here describes spiral bands as vortex Rossby waves. Within the vortex region, the theory is naturally suited for describing both inner and outer bands. Although gravity-inertia waves certainly account for some of the wave structures in a hurricane vortex, their dynamical significance is diminished in the absence of strong damping or critical levels. For non-stationary gravity-inertia waves with low vertical-mode number and horizontal wavelengths comparable to the radius of maximum winds, critical levels are unlikely when considering realistic hurricane vortices. In contrast, vortex Rossby waves are tied to the vortex and must eventually interact with it. This suggests an intimate link between spiral bands and hurricane evolution.

Chapter 6

CONCLUSION

The AB shallow water formulation presented here parallels the continuously stratified, baroclinic formulation of SM. The AB model has the potential of solving the scale problems associated with hurricane dynamics yet is simple enough to effectively illustrate fundamental processes. The internal consistency of the AB formulation was demonstrated by formulating conservation laws and diagnostic equations analogous to those of the linearized PE. Despite the formal divergence of the asymptotic series for $n \geq 2$ asymmetries in the near–core region, the zeroth order truncation was found to accurately evolve these wavenumbers on a stable, hurricane–like vortex. For these wavenumbers, the AB model was validated using a side–by–side comparison with analytical solutions for nondivergent vorticity dynamics.

The AB shallow water model has been further validated through a detailed analysis of wavenumber one evolution. Among the physical processes better understood is the manner by which wavenumber one moves the vortex. The analytical solution to the nondivergent model of GSM revealed that wavenumber one asymmetries project onto the pseudo mode through an interaction term. Reynolds stress plots of the AB model then give a physical interpretation to the interaction term. The steady pseudo mode emerges at long times and identifies the final position of the vortex. Understanding the transient dynamics and the pseudo mode suggests that it may be possible to easily diagnose storm motion in the linear model from the current geopotential field.

Detailed comparison of the AB model with an exact solution of the linearized nondivergent model demonstrated remarkable agreement. Agreement included radially propagating vorticity waves. Even specific measurements such as wave speed and location agree within a few percent.

To better understand the potential importance of vortex Rossby waves in vortex evolution and structure changes, an inviscid wave mechanics was developed. Expressions for the group velocity were derived using WKB theory. Radial wave-packet trajectories were consistent with AB simulations in regions of the vortex where the WKB assumptions were valid. Their dispersive nature and dependence on the vortex PV gradient justifies their designation as vortex Rossby waves.

The kinematics of individual wave packets show the existence of a stagnation radius which provides a site for wave mean-flow interaction. In the presence of convective forcing this process represents an asymmetric spin-up mechanism that could be operative in the formative stages of tropical cyclones. At later stages in the hurricane life cycle this process is consistent with the formation of secondary wind maxima.

In summary the wave mechanics developed here describes spiral bands as vortex Rossby waves. Within the vortex region, the theory is naturally suited for describing both inner and outer bands. Although gravity-inertia waves certainly account for some of the wave structures in a hurricane vortex, their dynamical significance is diminished in the absence of strong damping or critical levels. For non-stationary gravity-inertia waves with low vertical-mode number and horizontal wavelengths comparable to the radius of maximum winds, critical levels are unlikely when considering realistic hurricane vortices. In contrast, vortex Rossby waves are tied to the vortex and must eventually interact with it. This suggests an intimate link between spiral bands and hurricane evolution.

6.1 Suggested Future Work

In its current configuration, the AB model can move the grid in cases where the vortex motion is of interest. The insight gained in chapter 4 may simplify the grid moving algorithm or even make possible a "perfect" vortex–following algorithm for the linear model. Motion experiments in a variety of environmental flows could be carried out using the streamlined grid moving algorithm. The environmental flow could be complex and include synoptic features such as shortwaves. Being a balance formulation, the model numerics shouldn't be overly sensitive to the initial asymmetries or boundary conditions forced by the environment.

Weakly nonlinear terms may be added as a future enhancement. The model algorithm was developed with the capability to iterate on the geopotential tendency in anticipation of the nonlinear formulation. Observations indicate that the nonlinear terms should indeed be small (SM) and the model should therefore be well-suited for studies of inner-core vortex dynamics.

With the zeroth order AB formulation validated, the model could be extended to a two layer formulation. This would allow among other things, investigation of outflow layer dynamics.

REFERENCES

Abdullah, A. J., 1966: The spiral bands of a hurricane: a possible dynamic explanation. *J. Atmos. Sci.*, **23**, 367-375.

Barnes, G. M., E. J. Zipser, D. Jorgensen, and F. Marks, Jr., 1983: Mesoscale and convective structure of a hurricane rainband. *J. Atmos. Sci.*, **40**, 2125-2137.

Black, M. L., and H. E. Willoughby, 1992: The concentric eyewall of hurricane Gilbert. *Mon. Wea. Rev.*, **120**, 947-957.

Boyd, J.P., 1983: The Continuous spectrum of linear Couette flow with the Beta effect. *J. Atmos. Sci.*, **40**, 2303–2308.

Carr, L. E.,and R. T. Williams, 1989: Barotropic Vortex stability to perturbations from axisymmetry. *J. Atmos. Sci.*, **46**, 3177–3190.

Case, K. M., 1960: Stability of inviscid plane Couette flow. *Phys. Fluids*, **3**, 143-148.

Dritschel, D. G., and B. Legras, 1993: Modeling oceanic and atmospheric vortices. *Physics Today*, March, 44-51.

Eliassen, A., 1951: Slow thermally of frictionally controlled meridional circulation in a circular vortex. vortices. *Astrophys. Norv.*, **5**, 19-60.

Farrell, B., 1987: Developing disturbances in shear. *J. Atmos. Sci.*, **44**, 2191-2199.

Farrell, B. F., 1982: The initial growth of disturbances in a baroclinic flow. *J. Atmos. Sci.*, **39**, 1663-1686.

Franklin, J. L., S. J. Lord, S. E. Feuer,amd F. D. Marks, 1993: The kinematic structure of Hurricane Gloria (1985) determined from nested analyses of dropwindsonde and doppler radar data. *Mon. Wea. Rev.*, **121**, 2433-2451.

Fung, I. Y., 1977: The organization of spiral rainbands in a hurricane. *Massachusetts Institute of Technology* Ph.D. Thesis.

Gill, A. E., 1982: Atmosphere–Ocean Dynamics. (W. L. Dodd, ed.), pp. 496-497. Academic Press, Inc.

Guinn, T. A., and W. H. Schubert, 1992: Hurricane spiral bands. *J. Atmos. Sci.*, **50**, 3380-3403.

Kasahara, A., and G.W. Platzman,1963: Interaction of a hurricane with the steering flow and its effect upon the hurricane trajectory. *Tellus*, **15**, 321–335.

Kurihara, Y., 1976: On the development of spiral bands in a tropical cyclone. *J. Atmos. Sci.*, **33**, 940-958.

Leith, C. E., 1980: Nonlinear normal mode initialization and quasigeostrophic theory. *J. Atmos. Sci.*, **37**, 958–968.

MacDonald, N. J., 1968: The evidence for the existence of Rossby-like waves in the hurricane vortex. *Tellus* **XX**, 138-150.

May, P. T., 1995: The organization of convection in the rainbands of tropical cyclone Laurence. *Proceedings, 21st Conference on Hurricanes and Tropical Meteorology*, Miami, Florida, 233-234.

Pearce, R. P., 1993: A critical review of progress in tropical cyclone physics including experimentation with numerical models. *ICSU/WMO International Symposium on Tropical Cyclone Disasters*, Peking University Press, 45-60.

Pielke, R. A., W. R. Cotton, R. L. Walko, C. J. Trembach, W. A. Lyons, L. D. Grasso, and M. E. Nickolls, 1992: A comprehensive meteorological modeling system – RAMS. *J. Meteorol. Atmos. Phys.*, **49**, 69-91.

Powell, M. D., 1990: Boundary layer structure and dynamics in outer hurricane rainbands. Part I: Mesoscale rainfall and kinematic structure. *J. Atmos. Sci.*, **118**, 891-917.

Reznik, G. M., and W. K. Dewar, 1994: An analytical theory of distributed axisymmetric barotropic vortices on the β-plane. *J. Fluid Mech.*, **269**, 301-321.

Riehl, H., 1963: Some relations between wind and thermal structure of steady state hurricanes. *J. Atmos. Sci.*, **20**, 276–287.

Reznik, G. M., and W. K. Dewar, 1994: An analytical theory of distributed axisymmetric barotropic vortices on the β-plane. *J. Fluid Mech.*, **269**, 301-321.

Senn, H. V., and H. W. Hiser, 1959: On the origin of hurricane spiral rain bands. *Journal of Meteorology*, **16**, 419-426.

Shapiro, L. J., 1983: The asymmetric boundary layer flow under a translating hurricane. *J. Atmos. Sci.*, **40**, 1984-1998.

Shapiro L. J.,and K. V. Ooyama, 1990: Barotropic vortex evolution on a beta plane. *J. Atmos. Sci.*, **47**, 170–187.

Shapiro L. J.,and M. T. Montgomery, 1993: A three–dimensional balance theory for rapidly rotating vortices. *J. Atmos. Sci.*, **50**, 3322–3335.

Smith, G. B., and M. T. Montgomery, 1995: Vortex axisymmetrization and its dependence on azimuthal wavenumber or asymmetric radial structure changes. *Quart. J. Roy. Meteor. Soc.*, in press.

Smith, R. A., and M. N. Rosenbluth, 1990: Algebraic instability of hollow electron columns and cylindrical vortices. *Physical Review Letters* **64**, 649-652.

Smith, R. K., W. Ulrich, and G. Dietachmayer, 1990: A numerical study of tropical cyclone motion using a barotropic model. I: The role of vortex asymmetries. *Quart. J. Roy. Meteor. Soc.*, **116**, 337-362.

Sutyrin, G. G., 1989: Azimuthal waves and symmetrization of an intense vortex. *Sov. Phys. Doki.* **34**, 104-106.

Thomson, W., 1887: Stability of fluid motion: Rectilinear motion of viscous fluid between two parallel planes. *Phil. Mag.*, **24**, 188-196.

Tung, K. K., 1983: Initial-value problems for Rossby waves in a shear flow with critical level. *J. Fluid Mech.*, **133**, 443-469.

Tuttle, J. D., and B. Gall, 1995: Radar analysis of hurricanes Andrew and Hugo. *Proceedings 21st Conference on Hurricanes and Tropical Meteorology*, Miami, Florida, 608-610.

Willoughby, H. E., F. D. Marks Jr., and R. J. Feinberg, 1984: Stationary and moving convective bands in hurricanes. *J. Atmos. Sci.*, **41**, 3189-3211.

Willoughby, H. E., 1990a: Temporal changes of the primary circulation in tropical cyclones. *J. Atmos. Sci.*, **47**, 242–264.

Willoughby, H. E., 1990b: Gradient balance in tropical cyclones. *J. Atmos. Sci.*, **47**, 265–274.

Willoughby, H. E., 1992: Linear motion of a shallow–water barotropic vortex as an initial–value problem. *J. Atmos. Sci.*, **49**, 2015–2031.

Yamagata, T., 1976: On trajectories of Rossby wave-packets released in a lateral shear flow. *Journal of the Oceanographical Society of Japan*, **32**, 162-168.